Author **William D. Klopp**

1 General

Inconel MA 754 is the first oxide-dispersion-strengthened (ODS) nickel base alloy produced by the recently developed mechanical alloying process. It is primarily a solid solution alloy of 80Ni-20Cr which is further strengthened by Ti, Al carbides and, in particular, by a fine yttria dispersoid. The dispersoid imparts good strength and oxidation resistance to the alloy to temperatures of about 2000F, providing a service temperature advantage of up to several hundred degrees over other non-ODS superalloys. MA 754 has good fabricability in the fine-grained, as-extruded condition. It is usually given a final high temperature annealing treatment to produce a stable, recrystallized grain structure that is coarse and highly elongated in the direction of hot working. Grain aspect ratios can be as high as 10/1. This highly directional structure exhibits significant anisotropy in mechanical and physical properties. MA 754 is also strongly textured with the <100> crystallographic direction aligned parallel to the working direction. This textured structure results in a low modulus of elasticity in the longitudinal direction, giving improved resistance to thermal fatigue. MA 754 is of particular interest for high temperature components for advanced gas turbine engines such as vanes, shroud bands, fuel nozzles, and combustor hardware. It is currently used in several military aircraft engines. Industrial applications include molten glass processing, furnace fixtures, nuclear fuel cladding, and high temperature corrosion resistant parts (Refs. 1-6).

1.1 Commercial Designation

Inconel MA 754.

1.2 Alternate Designations

MA 754, Inconel Alloy MA 754, Alloy MA 754.

1.3 Specifications

1.4 Composition

1.4.1 *[Table]* Nominal composition.

	Ni
20.0	Cr
1.0	Fe
0.5	Ti
0.3	Al
0.05	C
0.6	Y_2O_3

1.5 Heat Treatment

The formation of large elongated grains is recognized as a crucial step in the development of superior high temperature properties in ODS alloys such as MA 754. This grain structure is developed through heat treatment to promote secondary recrystallization (exaggerated grain growth in alloys where the grain boundaries are initially pinned by a second phase). In the extruded and hot-rolled condition, MA 754 exhibits a fine-grained morphology with a slightly oblong grain shape. The dislocation density is high and the second phase particles exhibit a duplex distribution. Fine particles (presumably yttria) are uniformly distributed, while coarser particles (probably including titanium carbonitride) are oriented along the primary working direction. The secondary recrystallization response in MA 754 follows classic grain growth mechanisms and is primarily dependent on prior thermo-mechanical history. The transformation from a fine-grained to a coarse-grained structure does not occur at a single temperature but rather over a range of temperatures depending on prior processing. The transformation is also time-dependent, occurring as low as 1920F for a heating time of 200 hours (Ref. 7).

The standard secondary recrystallization heat treatment consists of 1 hour at 2400F, air cool (Ref. 1).

1.6 Hardness

1.6.1 *[Figure]* Effects of cold rolling and annealing on hardness.

1.6.2 *[Figure]* Effects of temperature on hot hardness.

1.7 Forms and Conditions Available

The standard form for MA 754 is hot-rolled, annealed flat bar in sizes ranging from 1 to 1.6 inch in thickness and from 2.8 to 6 inch in width. It is also available as plate, rod, rings, forgings, and sheet (Refs. 6-8).

1.8 Melting and Casting Practice

MA 754 is consolidated by the mechanical alloying (MA) process. This process, which was developed during the 1970's, involves extended dry milling of component powders in a high energy ball mill. At least one component powder must be ductile. A typical powder charge for MA 754 consists of 4 to 7 micron nickel powder, -150 micron chromium powder, -150 micron master alloy, and approximately 250-angstrom yttria powder. Master alloys are used primarily to introduce reactive additions such as aluminum and titanium into the mix. During milling, the particles are repeatedly fractured and rewelded with sufficient deformation to rupture any surface contaminant film and expose clean metal surfaces. The cold welding, which tends to increase the size of the particles involved, and fracturing, which tends to reduce particle size, reach a steady-state balance over time, leading to a relatively coarse but stable particle size. The internal structure of the particles, however, continues to be refined after the particle size stabilizes. Ultimately, each particle contains each of the alloy constituents in the original charged proportions, including a uniform dispersion of fine oxide particles. At this point, milling is complete and a uniform interparticle spacing of about 0.5 micron is achieved. The MA process allows the manufacture of specialized alloys having a combination of properties not attainable

in conventionally produced materials. For example, high temperature dispersion strengthening can be combined with a corrosion resistant matrix, such as has been done with MA 754.

ODS alloy powders such as MA 754 are highly cold worked and will not densify during simple sintering; they must be consolidated by a combination of high temperature and pressure, such as hot compaction plus hot extrusion, hot extrusion in a can, or hot isostatic pressing. Extrusion of canned powder is generally preferred. Processing after extrusion should be carefully controlled to produce the proper grain structure for the intended application. The fine-grained structure which is characteristic of extruded material gives the best room temperature strength, fatigue strength, and workability for subsequent forming. In contrast, the coarse, elongated grain structure developed by secondary recrystallization of thermo-mechanically processed material gives the best high temperature strength and thermal fatigue resistance. The latter structure is preferred for most high temperature applications (Refs. 1, 2, 4, 9, 10, 11).

1.9 Special Considerations

1.9.1 Although MA 754 has excellent resistance to oxidation at elevated temperatures, subsurface chromium loss occurs on oxidation exposure at and above about 2000F. This chromium loss, which is associated with oxidation, causes formation of internal voids and consequent decrease in strength properties. The loss becomes more severe with increasing time and temperature of exposure (see Section 2.3.4).

1.9.2 Volatilization of the chromia scale occurs in high velocity oxidizing environments above about 1832F (see Section 2.3.4.7).

1.9.3 High temperature tensile strength, stress-rupture strength, and fatigue strength are highly dependent on orientation with respect to the fabrication direction and alignment of the large, elongated grain structure produced by the final standard heat treatment at 2400F. Strength properties are best in the longitudinal direction and are progressively decreased in the long transverse and short transverse directions. The orientation effect on strength properties can be alleviated by controlling fabrication procedures to produce less directional grain structures (see Sections 3.3, 3.4, and 3.5).

1.9.4 The resistance of MA 754 to thermal fatigue cracking is orientation dependent. While the resistance to transverse cracking (along longitudinal edges) is excellent, the resistance to longitudinal cracking is less than that of other superalloys (see Section 3.5.4).

1.9.5 Special care is required in joining. The use of fusion welding techniques destroys the unique microstructure responsible for the high temperature strength of MA 754. Accordingly, fusion welds that are needed for attachment or positioning for brazing should be located in areas of relatively low stress. Non-fusion joining processes can produce joint strengths approaching those of the parent metal. Liquid phase diffusion bonding and brazing are suitable for assembly of aircraft engine components (see Section 4.3).

2 Physical Properties and Environmental Effects

2.1 Thermal Properties

2.1.1 Melting Range. Approximate solidus 2550F (Ref. 6).

2.1.2 Phase Changes. During the course of processing and heat treatment, the yttria dispersoid increases in size and changes composition by reaction with aluminum. In one study (Ref. 13), the average particle diameter for the starting as-calcined yttria powder was determined as about 90 angstroms, increasing to roughly 130 angstroms after mechanical alloying and annealing for 2 hours at 2400F. Annealing for an additional 70 hours at 2372F increased the average dispersoid diameter to 230 angstroms. Four mixed aluminum-yttrium oxides have been identified in the processed alloy in addition to aluminum oxide. These oxides are: YAG, $5Al_2O_3 \cdot 3Y_2O_3$ (cubic); YAP, $Al_2O_3 \cdot Y_2O_3$ (orthorhombic); YAP', $Al_2O_3 \cdot Y_2O_3$ (monoclinic); and YAM, $Al_2O_3 \cdot 2Y_2O_3$ (monoclinic) (Refs. 9, 12). Larger particles, which include titanium carbonitride, are also present in the microstructure. These larger particles grow with annealing time at 2400F when located at grain boundaries but not within the grains, as shown in Figure 2.1.2.1 (Ref. 14).

2.1.2.1 *[Figure]* Effect of annealing time at 2400F on particle size at grain boundaries and within grains.

2.1.2.2 Time-temperature-transformation diagrams.

2.1.3 Thermal Conductivity.

2.1.3.1 *[Figure]* Thermal conductivity.

2.1.4 Thermal Expansion.

2.1.4.1 *[Figure]* Mean coefficient of linear thermal expansion.

2.1.5 Specific Heat.

2.1.5.1 *[Figure]* Specific heat.

2.1.6 Thermal Diffusivity.

2.2 Other Physical Properties

2.2.1 Density. 0.30 lb/cu in., 8.3 g/cc (Ref. 6).

2.2.2 Electrical Properties.

2.2.2.1 *[Figure]* Electrical resistivity.

2.2.3 Magnetic Properties. Relative permeability at 200 oersteds at 70F is 1.001 (Ref. 6).

2.2.4 Emittance.

2.2.5 Damping Capacity.

2.3 Chemical Environments

2.3.1 General Corrosion.

2.3.2 Stress Corrosion.

2.3.3 Hydrogen Effects (see Table 3.2.7.1.1).

2.3.4 Oxidation. The presence of yttria in MA 754 effects a significant improvement in high temperature oxidation resistance. This improvement is shown in Figure 2.3.4.1, where the oxidation weight gain behavior of MA 754 is compared to that of a similar non-ODS alloy of Ni-25Cr. At 1832F, the scale on MA 754 is adherent, while the Ni-25Cr alloy oxidizes more rapidly and begins to spall after about 100 hours. At 2012F, MA 754 begins to spall after 100 hours, while spalling occurs on Ni-25Cr after about 15 hours. The scale compositions also show important differences. The Ni-25Cr alloy scale is largely Cr_2O_3 with small amounts of $NiCr_2O_4$ and traces of NiO. In contrast, the scale on MA 754 consists entirely of Cr_2O_3 (with small amounts of dissolved yttrium). Detailed studies of transport mechanisms in the chromia-rich oxide show that the scale grows by a combination of both cation and anion diffusion. Reduced outward scale growth is a major effect of yttrium, with a larger proportion of the scale resulting from inward growth than is observed for non-yttria-containing alloys. Yttria causes a suppression of cation transport and enhancement of oxygen diffusion, leading to oxide scales which grow almost exclusively by grain boundary oxygen transport (Refs. 15-18).

2.3.4.1 *[Figure]* Oxidation weight changes in air for MA 754 and a model alloy Ni-25Cr.

2.3.4.2 *[Figure]* Oxidation weight change behavior at 1832F for times up to 5000 hours.

2.3.4.3 *[Figure]* Oxidation weight change behavior at 1832F and 2012F for times up to 1000 hours.

2.3.4.4 [Figure] Oxidation weight change behavior at 1832 to 2192F.

2.3.4.5 *[Table]* Cyclic oxidation resistance at 2012F for MA 754, Inconel 713C, and IN-738.

Subsurface chromium depletion and associated void formation occur during oxidation of MA 754 at 2012 to 2192F. The extent of chromium depletion and the number and size of voids increases with increasing exposure time (based on measurements after exposures of 1 to 100 hours) and temperature. Chromium depletion at the surface approximates 10 percent when measured along a line parallel to the elongated grain structure and 5 percent when measured along a perpendicular line, as shown in Figure 2.3.4.6. The diffusivity of chromium in MA 754 at 2192F is calculated from these microprobe data to be $4 \times 10^{-10} cm^2/sec$. Observations on Ni-20Cr and Ni-30Cr samples exposed similarly indicate that void formation is not related to the presence of yttria in MA 754 but rather is a result of the high temperature oxidation reaction in Ni-Cr alloys (Ref. 19).

2.3.4.6 *[Figure]* Microprobe traces of chromium content after oxidation exposure in air for 100 hours at 2192F.

2.3.4.7 The chromia-rich scale which forms on MA 754 during high temperature exposure in an oxidizing atmosphere is subject to loss by volatilization. It is considered unsuitable for use in high gas velocity applications at temperatures above 1832F where the chromia scale is needed for oxidation protection (Ref. 20).

The yttria dispersoid also promotes improved oxidation resistance in atmospheres other than air. As compared to non-yttria-containing Ni-30Cr and Ni-30Cr-0.5Ti alloys, MA 754 oxidizes 12 to 14 times slower in an $80CO\text{-}20CO_2$ mixture at 1832 to 2057F. Experimental evidence suggests, as it does during air oxidation, that yttrium dissolves in the chromia scale and acts as a donor, decreasing the population of chromium interstitials and suppressing thereby the flux of chromium through the scale during high temperature oxidation (Ref. 21).

In an $H_2\text{-}45CO_2\text{-}1H_2S$ environment, MA 754 showed only minimal weight gain after 1008 hours at 1500F. However, in the same test environment at 1800F, MA 754 exhibited breakaway oxidation-sulfidation after 1440 hours (Ref. 22).

2.3.4.8 *[Table]* Burner rig oxidation resistance at 1700F for MA 754 and four other superalloys.

2.3.4.9 *[Figure]* Depth of metal loss and maximum attack after burner rig testing for 500 hours at 1700F for MA 754 and two other superalloys.

The hot corrosion of MA 754 and of a similar alloy composition without yttria has been studied in salt mixtures of Na_2SO_4/NaCl, with weight loss results as shown in Figure 2.3.4.10. MA 754 exhibited higher corrosion rates at 1652 to 2012F and in particular at 1832F and NaCl contents between about 25 and 75 percent. Internal penetration by the molten salt was observed with both alloys but was two-fold to three-fold greater in the longitudinal direction than in the transverse direction for MA 754 at 1652 and 1832F. There was little internal penetration at 2012F. The poorer corrosion resistance of MA 754 as compared to the non-yttria-containing alloy is attributed to its coarser grain structure (Ref. 23).

2.3.4.10 *[Figure]* Effects of salt composition and temperature on the corrosion weight loss of Ni-20Cr-0.3Al-0.5Ti and MA 754 alloys exposed for 16 hours in Na_2SO_4-NaCl mixtures.

2.4 Nuclear Environments

3 Mechanical Properties

3.1 Specified Mechanical Properties

3.2 Mechanical Properties at Room Temperature

3.2.1 Tension Stress-strain Diagrams and Tensile Properties.

3.2.2 Compression Stress-strain Diagrams and Compression Properties.

3.2.3 Impact.

3.2.3.1 *[Table]* Effects of orientation on impact energy at room temperature.

3.2.4 Bending.

3.2.5 Torsion and Shear.

3.2.6 Bearing.

3.2.7 Stress Concentration.

3.2.7.1 Notch properties.

3.2.7.1.1 *[Table]* Effects of notches on room temperature tensile properties in helium and in hydrogen.

3.2.7.2 Fracture toughness.

3.2.8 Combined Loading.

3.3 Mechanical Properties at Various Temperatures

3.3.1 Tension Stress-strain Diagrams and Tensile Properties. High strength at elevated temperatures is the prime characteristic of interest for MA 754. Oxide dispersion strengthening associated with the yttrium oxide dispersoid is effective at temperatures up to the melting point of the alloy. The high-aspect-ratio grain structure developed by thermo-mechanical processing also contributes to high-temperature strengthening. The highly directional structure leads to anisotropy in mechanical properties, apparent in both short-time tensile and longer-time creep and rupture properties (Ref. 6).

3.3.1.1 *[Figure]* Longitudinal tensile properties of thermo-mechanically processed bar.

3.3.1.2 *[Figure]* Long transverse tensile properties of thermo-mechanically processed bar.

3.3.1.3 *[Figure]* Longitudinal tensile properties of hot rolled and annealed bar.

3.3.1.4 *[Figure]* Transverse tensile properties of hot rolled and annealed bar.

3.3.1.5 *[Figure]* Effects of strain rate and temperature on yield strength.

3.3.1.6 *[Figure]* Effects of strain rate and orientation on tensile strength at 1400F.

In the as-rolled, fine-grained condition, MA 754 is considerably weaker than in the annealed, large-grained condition, as seen by comparison of flow stresses for fine-grained alloy in Figure 3.3.1.7 with creep stresses for coarse-grained alloy at similar deformation rates and temperatures in Figures 3.4.2, 3.4.4, and 3.4.6. The fine-grained alloy is not superplastic but shows excellent ductility at intermediate strain rates at 1832F, as shown in Figure 3.3.1.8. These tensile properties indicate good formability in the fine-grained condition (Refs. 24, 25).

3.3.1.7 *[Figure]* Effects of strain rate and temperature on flow stress of fine-grained MA 754.

3.3.1.8 *[Figure]* Effects of strain rate on strain rate sensitivity and ductility for fine-grained MA 754 at 1832F.

3.3.2 Compression Stress-strain Diagrams and Compression Properties.

3.3.2.1 *[Figure]* Compression stress-strain curves at room and elevated temperatures.

3.3.2.2 The yield and flow stresses in compression are seen to be considerably higher for MA 754 than for Nimonic 75 (a non-ODS alloy with similar composition as the MA 754 matrix), as shown in Figures 3.3.2.3 and 3.3.2.4. The strength increment due to dispersoid particles can be accounted for by use of a threshold stress in the creep (flow) equation:

$$\dot{\varepsilon} = K (\sigma_A - \sigma_{TH})\, n_o$$

where $\dot{\varepsilon}$ = steady creep (or flow) rate

σ_A = applied stress

σ_{TH} = threshold stress due to particles

n_o = stress exponent of particle-free matrix

K = proportionality constant

The threshold stress for MA 754 at 1562F is estimated from these data as 23 ksi (Ref. 26).

3.3.2.3 *[Figure]* Effects of temperature on compressive 0.2-percent yield strengths of MA 754 and of non-ODS alloy Nimonic 75.

3.3.2.4 *[Figure]* Effects of strain rate on steady-state flow stress in compression at 1562F for MA 754 and non-ODS alloy Nimonic 75.

3.3.3 Impact.

3.3.4 Bending.

3.3.5 Torsion and Shear.

3.3.6 Bearing.

3.3.7 Stress Concentration.

3.3.7.1 Notch properties.

3.3.7.2 Fracture toughness.

3.3.8 Combined Loading.

3.4 Creep and Creep Rupture Properties

The high temperature deformation of MA 754 is characterized by two distinct regions of creep and stress-rupture behavior, as shown in Figures 3.4.1 to 3.4.4. At high stresses, the power dependency of creep is unusu-

ally high, about 30 to 40, and dislocation creep is observed. The high-stress creep behavior of ODS alloys such as MA 754 is usually considered in terms of an effective stress, the applied stress less a threshold stress below which creep does not occur (see equation in Section 3.3.2.2). The introduction of the threshold stress brings the stress exponent in the creep equation down from 30 to 40 to values of 4 to 7, which would be characteristic of the particle-free matrix. The threshold stress is considered related to dislocation pinning at oxide particles.

At lower applied stresses, the stress exponents are low and fracture is intergranular. In this regime the stress exponent depends strongly on grain morphology. Heat 1 (Figures 3.4.1 and 3.4.2), with a uniform fiber grain morphology, exhibited stress exponents of 5 to 16. Small dispersoid-free zones formed adjacent to cavities at transverse grain boundaries; the growth of these cavities is believed to be diffusion-controlled. Heat 2, which was weaker and had a duplex grain morphology consisting of coarse grains with packets of fine equiaxed grains, had stress exponents of 1.6 and 2.5 at 2000 and 2192F, respectively. The presence of fine grains allows grain boundary sliding to occur during creep. The presence of fine recrystallized grains is weakening at high temperatures and low stresses; processing should be tailored as best possible to produce a uniformly fibered grain structure. Similar behavior is indicated by the data in Figures 3.4.3 and 3.4.4. Here, Bar No. 1 was large-grained while Bars Nos. 2 and 3 were fine-grained and more equiaxed; the latter were weaker than Bar No. 1 at longer times and higher temperatures (Refs. 14, 27, 28, 29, 30, 31).

3.4.1 *[Figure]* Effects of temperature and grain structure on stress-rupture behavior of two heats of MA 754.

3.4.2 *[Figure]* Effects of temperature and grain structure on creep behavior of two heats of MA 754.

3.4.3 *[Figure]* Effects of temperature and grain structure on stress-rupture behavior of two bars of MA 754.

3.4.4 *[Figure]* Effects of temperature and grain structure on creep behavior of two bars of MA 754.

The elevated temperature stress-rupture properties of MA 754 bar are highly dependent on testing direction, as indicated in Figures 3.4.5 and 3.4.6 and Table 3.4.7. The rupture stress capability in the longitudinal direction is consistently higher than in the transverse direction, and the strength difference increases with increasing temperature. This behavior reflects the differences in grain aspect ratio in the two directions; the elongated grain structure presents more grain boundary area normal to the applied stress when tested in the transverse direction than in the longitudinal direction (Refs. 9, 32).

3.4.5 *[Figure]* Effects of temperature and orientation on stress-rupture behavior of two heats of MA 754.

3.4.6 *[Figure]* Effects of temperature and orientation on creep behavior of two heats of MA 754.

3.4.7 *[Table]* Longitudinal and long transverse stress-rupture properties.

3.4.8 *[Figure]* Time of 0.5 percent creep strain.

3.4.9 *[Figure]* Time to 1.0 percent creep strain.

3.4.10 *[Table]* Elevated temperature stress-rupture strength of MA 754 and other superalloys.

3.4.11 *[Figure]* Similarity of creep and tensile flow behavior at elevated temperatures.

The stress-rupture behavior of MA 754 is insensitive to prior 100 hour exposures at 1832F in either air or vacuum. The insensitivity of MA 754 to prior exposure is attributed to its intrinsic brittleness (less than 2 percent reduction in area in stress-rupture tests at 1292 to 1832F), the grain boundaries being pinned by the dispersed oxide (Ref. 33). However, the creep behavior at 1400F is sensitive to prestraining at 1400F, as shown in Figure 3.4.12 (Ref. 34).

3.4.12 *[Figure]* Effect of prestraining on minimum creep rate at 32.5 ksi and 1400F.

Creep crack-growth rates at 1832F are higher in the T-L orientation than the L-T orientation in both air and vacuum, as shown in Figure 3.4.13. Also, the apparent threshold stress intensity for creep crack growth is much lower for the T-L orientation than for the L-T orientation. Faster crack growth in the T-L orientation may be related to creep voids on particles aligned parallel to the growth direction, facilitating crack extension. The orientation effect is much larger in creep than in fatigue, as seen by comparison of creep crack-growth rates in Figure 3.4.13 with fatigue crack-growth rates in Figure 3.5.3.4 (Ref. 35).

3.4.13 *[Figure]* Effects of orientation and environment on creep crack-growth rate at 1832F.

3.4.14 *[Figure]* Shear and tensile rupture strengths at 1400F.

3.5 Fatigue Properties

3.5.1 Conventional High-Cycle Fatigue. The high-cycle fatigue (HCF) behavior, which is important for gas turbine design, has been studied at 1562F in air. The anisotropy of grain shape and high degree of texture in MA 754 causes HCF properties to be strongly orientation dependent. As seen in Figure 3.5.1.1, the longitudinal specimens have the highest fatigue strength, short transverse have the lowest, and long transverse specimens show an intermediate fatigue strength. Subsurface porosity resulting from high temperature oxidation exposure also can affect HCF. The non-spherical voids generally form as stringers aligned parallel to the longitudinal direction of the grains with a tendency to lie along grain boundaries. Figure 3.5.1.2 shows that air exposure has no significant effect on HCF strength in the longitudinal direction but strongly reduces fatigue

strength in the long transverse direction. This behavior is attributed to the exaggerated effect of void acuity on stress intensity for voids with their long axes normal to the applied stress (Refs. 36, 37).

3.5.1.1 *[Figure]* Effects of specimen orientation on high-cycle fatigue behavior at 1562F.

3.5.1.2 *[Figure]* Effects of high temperature air exposure on high-cycle fatigue behavior at 1562F for two specimen orientations.

3.5.1.3 *[Figure]* Longitudinal rotating-beam fatigue strength.

3.5.1.4 *[Figure]* Long transverse rotating-beam fatigue strength.

3.5.2 Low-Cycle Fatigue. The strain-controlled low-cycle fatigue behavior of MA 754 is shown in Figure 3.5.2.1. The fatigue strength decreases normally with increase in test temperature from 1382 to 2012F. Crack initiation occurs either on the specimen surface, usually as a result of environmental attack of surface-connected grain boundaries or within the specimen interior, in which case it is due to the presence of recrystallization defects consisting of fine grains within the large-grained microstructure. Elimination of these recrystallization defects may improve high temperature fatigue properties by reducing premature crack initiation (Ref. 38).

3.5.2.1 *[Figure]* Effect of temperature on low-cycle fatigue behavior.

The high temperature low-cycle fatigue behavior of MA 754 is dependent on specimen orientation and type of strain cycle. As shown in Figure 3.5.2.2, longitudinal specimens generally exhibit longer lives than long transverse specimens. Strain cycles with tensile-only hold times are most damaging to the fatigue lives of both orientations. In contrast, longitudinal specimens tested under cycles with only compressive holds or with both tensile and compressive holds exhibited similar or improved fatigue behavior as compared to strain cycles with no holds. The improvement in fatigue life associated with compressive holds is attributed to the healing effect of compressive creep (Ref. 39).

3.5.2.2 *[Figure]* Effects of specimen orientation and strain wave form on low-cycle fatigue behavior at 1562F.

3.5.2.3 *[Figure]* Cyclic stress-strain curves.

Strain-controlled low-cycle fatigue (LCF) at 1562F and thermal-mechanical fatigue (TMF) at 752 to 1562F produce similar lifetimes for similar elastic, inelastic, and total (thermal plus mechanical) strain ranges, as shown in Figure 3.5.2.4. Crack initiation was transgranular in all cases. Crack propagation was transgranular during LCF and mixed inter- and transgranular in TMF (Ref. 40).

3.5.2.4 *[Figure]* Low-cycle fatigue behavior at 1562F and thermal-mechanical fatigue behavior at 752 to 1562F.

3.5.3 Fatigue Crack Propagation. Fatigue crack-growth rates, shown in Figure 3.5.3.1, are dependent on both specimen orientation and frequency. Crack-growth rates are lower for longitudinal than for long transverse specimens. Also, the crack propagation rates for longitudinal specimens increase as the frequency is decreased from 50 to 0.5 cps. The effect of load ratio on the threshold stress intensity factor is shown in Figure 3.5.3.2. The threshold stress intensity factor is slightly greater for longitudinal than for long transverse specimens and decreases with increasing load ratio. The strongly anisotropic fatigue behavior of MA 754 is attributed to differences in the ease of crack initiation and growth associated with the grain structure directionality. In longitudinal specimens, crack initiation and propagation occur primarily transgranularly, while in short transverse specimens, these processes occur intergranularly. The transverse specimens are more prone to intergranular crack initiation and growth since there is a larger grain boundary area normal to the applied stress. The fatigue life behavior of MA 754 is more closely related to crack initiation than to crack propagation (Refs. 36, 37).

3.5.3.1 *[Figure]* Effects of cycle frequency and specimen orientation on fatigue crack-growth rates at 1562F.

3.5.3.2 *[Figure]* Effects of load ratio and specimen orientation on threshold stress intensity factor for fatigue crack propagation at 1652F.

Further effects of temperature, orientation, and waveform on low-cycle fatigue crack growth behavior are shown in Figures 3.5.3.3 and 3.5.3.4. The effect of orientation changes as the temperature increases. At room temperature and low stress intensity factor ranges, crack-growth rates for the T-L orientation are slightly lower than those for the L-T orientation. However, at 1400F, crack-growth rates are considerably higher for the T-L orientation, while at 1832F rates for the two orientations are about equal. A one-minute tensile hold in the fatigue cycle raises the growth rate appreciably, indicating that crack growth is sensitive to both time and cycles. In the L-T orientation, significant cracking occurs normal to the direction of the main crack to the extent that final fracture can occur in that direction. In vacuum, secondary cracking retards crack growth (Ref. 35).

3.5.3.3 *[Figure]* Effects of temperature and specimen orientation on fatigue crack-growth rates in air.

3.5.3.4 *[Figure]* Effects of hold time, environment, and orientation on fatigue crack-growth rates at 1832F.

3.5.4 Thermal Fatigue. The resistance of MA 754 to transverse thermal fatigue cracking is excellent compared to that of conventionally cast superalloys, as shown in Figure 3.5.4.1. (The design in these tests allowed observation only of cracks transverse to the long dimension

on the specimen.) The improvement is attributed primarily to the <100> crystallographic orientation of MA 754 and low elastic modulus in the longitudinal direction. Directionally solidified superalloys and a group of experimental Ni-16Cr-4.5Al-Y_2O_3 ODS alloys have similar crystallographic orientation and also exhibit superior thermal fatigue resistance as compared to the conventionally cast superalloys, which have a randomly oriented crystallographic structure. The presence of transverse grain boundaries in the MA 754 and other ODS alloys does not adversely affect thermal fatigue resistance, as seen by comparison with the directionally solidified alloys, which do not have transverse grain boundaries. Only minor benefit was afforded by the NiCrAlY coating, which on MA 754 tended to peel and flake during testing (Refs. 41, 42).

3.5.4.1 *[Figure]* Thermal fatigue behavior at 2065F for MA 754 compared with other types of superalloys.

Additional results from another study using a slightly different specimen design provide information on both longitudinal and transverse thermal cracking. These data, shown in Table 3.5.4.2, confirm that MA 754 has good resistance to transverse thermal fatigue cracking, slightly better than that of directionally solidified X-40 but inferior to that of the high strength René 150 alloy. In the longitudinal direction, however, the thermal cracking resistance of MA 754 is reduced to below that of both X-40 and René 150. The reduced resistance to longitudinal thermal fatigue cracking in MA 754 is attributed to strain-induced cavitation at oxide particles and limited transverse ductility (Refs. 42, 43).

3.5.4.2 *[Table]* Thermal fatigue behavior at 1787 and 1967F for MA 754 compared to two other superalloys.

3.6 Elastic Properties

3.6.1 Poisson's Ratio.

3.6.2 Modulus of Elasticity. The modulus of elasticity varies with the degree of crystallographic texture imparted to the material during hot working. For applications requiring good resistance to longitudinal thermal fatigue, the alloy is processed to a textured structure which has a low modulus of elasticity in the longitudinal direction. In this condition, MA 754 has a longitudinal modulus of 20 to 25x10^3 ksi at room temperature, with typical values at higher temperatures as shown in Figure 3.6.2.1. Without special processing, room temperature modulus values for both longitudinal and transverse specimens range from 28 to 32x10^3 ksi, with higher temperature values shown also in Figure 3.6.2.1 (Ref. 6).

3.6.2.1 *[Figure]* Modulus of elasticity as a function of temperature.

3.6.3 Modulus of Rigidity.

3.6.4 Tangent Modulus.

3.6.5 Secant Modulus.

4 Fabrication

4.1 Forming

Typical fabrication steps include encapsulation of mechanically alloyed powder in a steel can, extrusion at 700F, and hot forming at 1700 to 2000F. The fine-grained extruded bar can be coined, upset, and forged, or precision forged directly to specialized shapes such as vanes and blades which are then recrystallized to a coarse, elongated grain structure with the desired <100> texture. MA 754 can also be formed by hot spinning and ring rolling. Bar and plate can be produced by hot rolling (see Figures 3.3.1.3 and 3.3.1.4). Processing conditions should be carefully controlled to give the optimum final microstructure and associated mechanical properties for the intended application. For example, the strength differential between the longitudinal and transverse directions in plate can be reduced by cross-rolling to produce coarse equiaxed pancake-shaped grains. In the fully cross-rolled condition, equal longitudinal and transverse stress-rupture properties are observed, the strength being about 80 percent of that for longitudinal bar (Refs. 2, 9, 44).

4.2 Machining and Grinding

MA 754 can be machined readily by conventional procedures for high-nickel alloys. The alloy should be machined in the recrystallized condition (Ref. 11).

4.3 Joining

MA 754 can be joined by liquid phase diffusion bonding to produce joints with good strength retention to elevated temperatures. Laboratory tests have been conducted using experimental Ni-20Cr alloys containing boron, silicon, and/or germanium to depress the melting points to between 1840 and 1900F (compared to 2540F for 80Ni-20Cr). Specimens of MA 754 were joined by inserting a thin 0.8 mil strip of bonding alloy between mating faces and heating for 1 to 20 hours at 2192F. Although there was some coagulation of yttria particles at the bond interface, the joint structures were sound without voids. Good tensile properties were maintained up to at least 1652F, as shown in Figure 4.3.1. The stress-rupture life at 1832F of the bonded alloy was more than 85 percent of that of the base alloy, Figure 4.3.2, indicating the viability of this joining method (Ref. 45, 46).

4.3.1 *[Figure]* Effects of temperature on tensile strength and elongation of liquid phase diffusion bonded alloy.

4.3.2 *[Figure]* Stress-rupture strength of liquid phase diffusion bonded alloy at 1800F.

MA 754 can be brazed for structural applications up to 2000F. A study of three commercial braze alloys showed that AM788 was the most versatile alloy to use with MA 754 based on its moderate brazing temperature and good stress-rupture strength of brazed joints at 1800 and 2000F, as shown in Table 4.3.3. Brazing alloy B93 also produced strong joints at 1800F. Joints made with brazing alloy TD6 had good strength at 2000F, but exhibited micro-porosity and thus were less attractive (Ref. 47).

4.3.3 *[Table]* Stress-rupture properties of brazed joints.

Fusion welding is not feasible for structural applications because the oxide dispersion is rendered ineffective or lost through agglomeration or slagging during welding (Ref. 47).

MA 754 can be resistance spot welded for fixturing prior to brazing (Ref. 47).

Riveting with rivets of similar composition has been employed successfully for non-aircraft applications (Ref. 9).

An evaluation of braze repair techniques for gas turbine engine nozzles has indicated that B93 and AM788 are the best braze alloys for MA 754 out of thirteen evaluated, based on amount of brittle second phase formed in the braze region, melt erosion of the original alloy, and porosity (see braze compositions in Table 4.3.3) (Ref. 48).

4.4 Surface Treating

Table 1.4.1 Nominal composition (Ref. 6)

Alloy: MA 754	
Component	**Percent**
Chromium	20
Iron	1.0
Titanium	0.5
Aluminum	0.3
Carbon	0.05
Yttrium Oxide(Y_2O_3)	0.6
Nickel	Balance

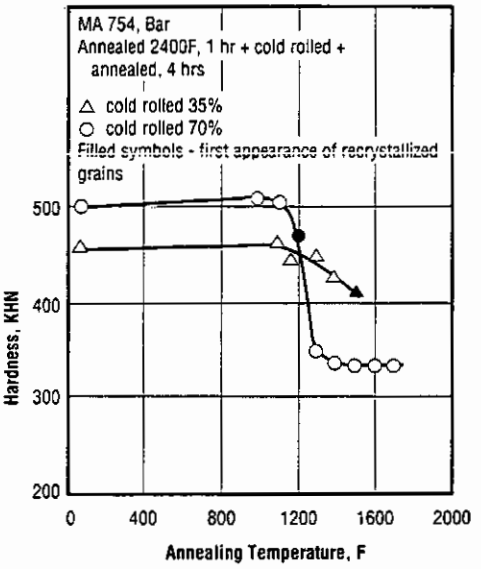

Fig. 1.6.1 Effects of cold rolling and annealing on hardness (Ref. 14)

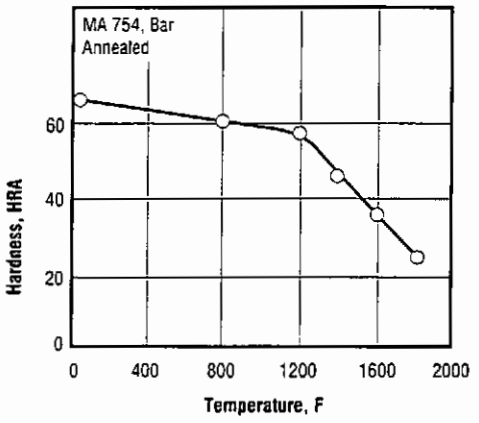

Fig. 1.6.2 Effects of temperature on hot hardness (Ref. 6)

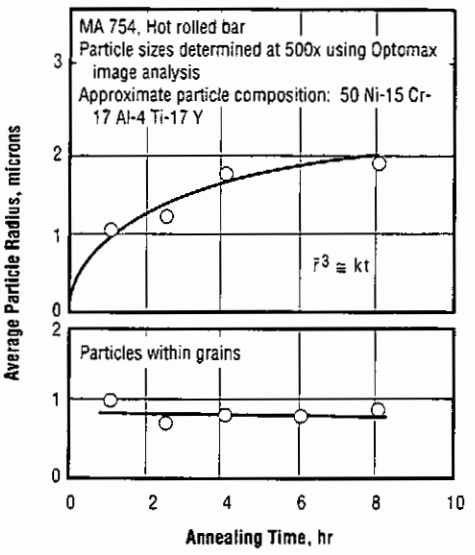

Fig. 2.1.2.1 Effect of annealing time at 2400F on particle size at grain boundaries and within grains (Ref. 14)

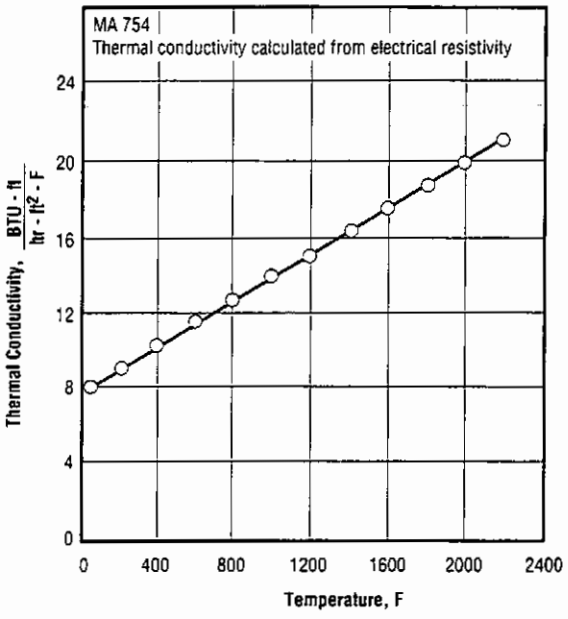

Fig. 2.1.3.1 Thermal conductivity (Ref. 6)

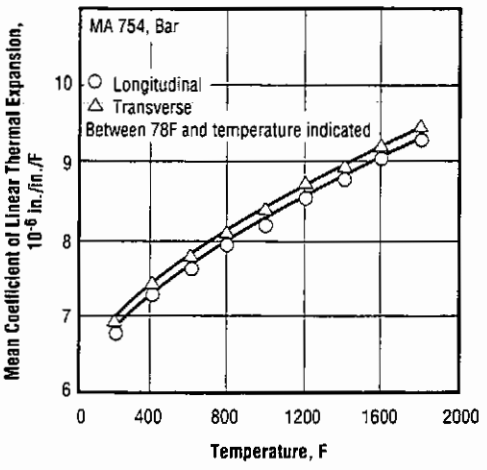

Fig. 2.1.4.1 Mean coefficient of linear thermal expansion (Ref. 6)

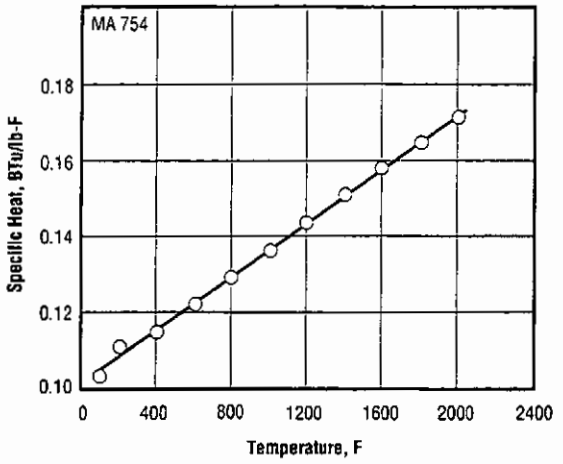

Fig. 2.1.5.1 Specific heat (Ref. 6)

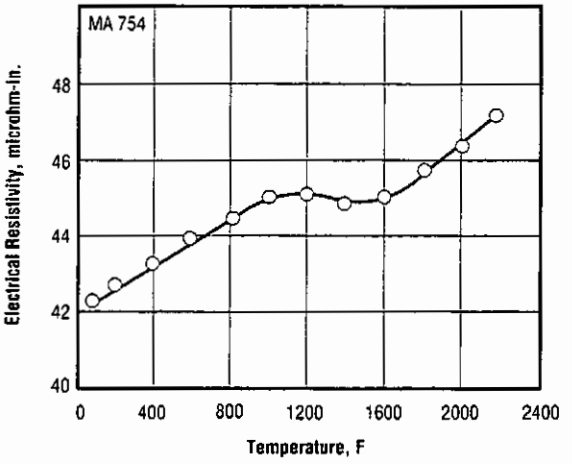

Fig. 2.2.2.1 Electrical resistivity (Ref. 6)

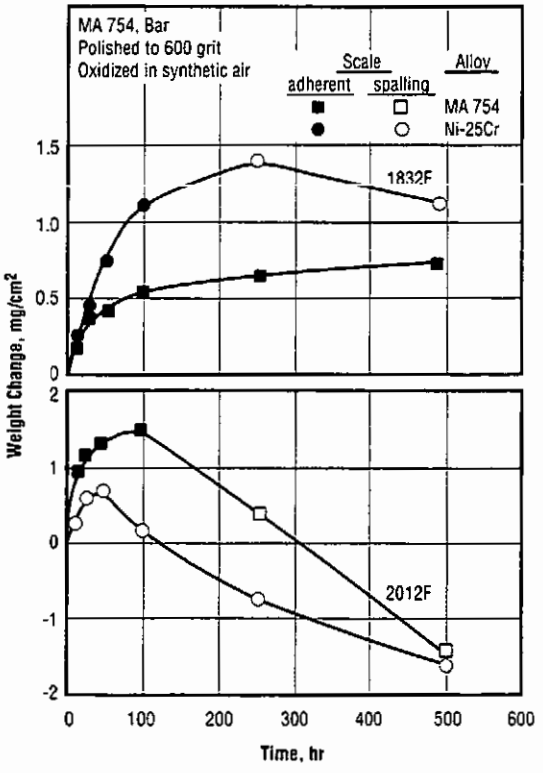

Fig. 2.3.4.1 Oxidation weight changes in air for MA 754 and a model alloy Ni-25Cr (Ref. 18)

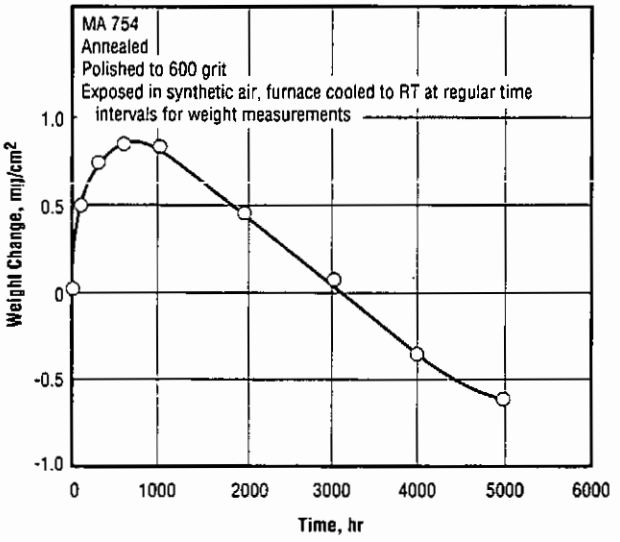

Fig. 2.3.4.2 Oxidation weight change behavior at 1832F for times up to 5000 hrs (Ref. 16)

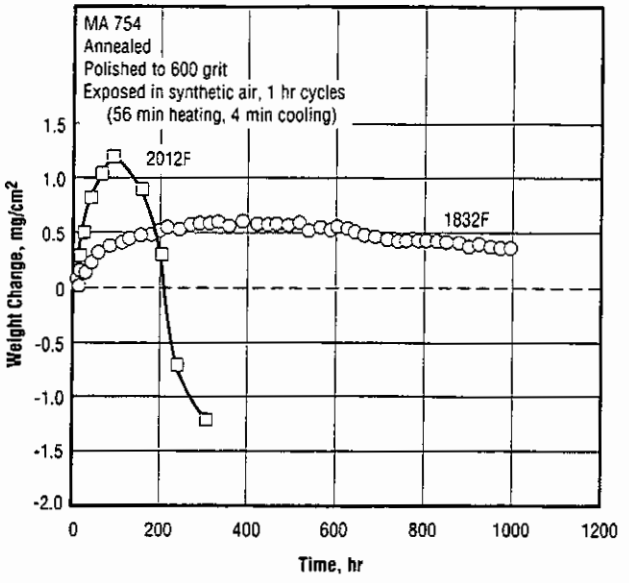

Fig. 2.3.4.3 Oxidation weight change behavior at 1832F and 2012F for times up to 1000 hrs (Ref. 16)

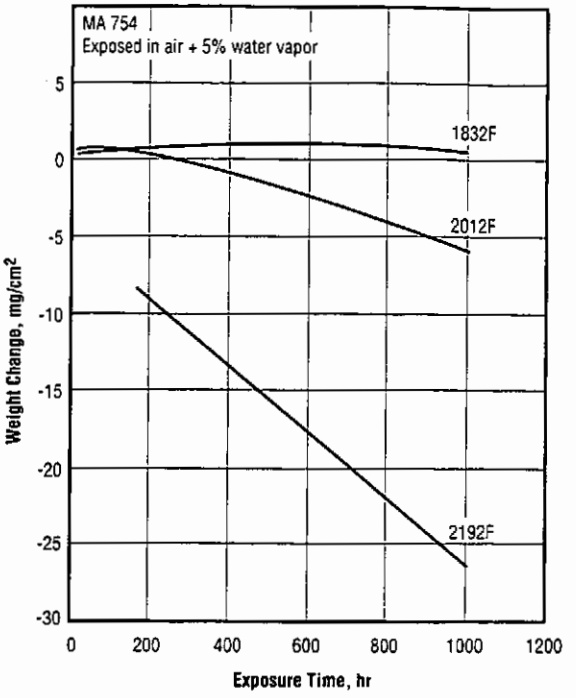

Fig. 2.3.4.4 Oxidation weight change behavior at 1832F to 2192F (Refs. 9, 22)

Table 2.3.4.5 Cyclic oxidation resistance at 2012F for MA 754, Inconel 713C, and IN-738 (Ref. 6)

Alloy	Weight Change, mg/cm²	
	Undescaled	Descaled
Inconel MA 754	-2.5	-7.2
Inconel 713C	-19.2	-21.1
IN-738	-70.9	-78.1

Note: Alloys exposed for 504 hours in air with 5 percent H_2O, thermal cycled by rapid cool to room temperature every 24 hours.

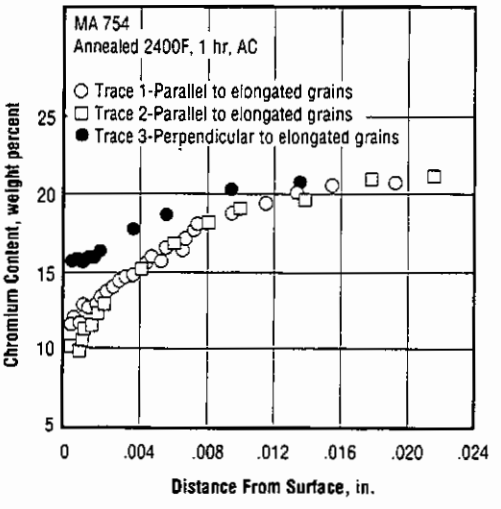

Fig. 2.3.4.6 Microprobe traces of chromium content after oxidation exposure in air for 100 hours at 2192F (Ref. 19)

Table 2.3.4.8 Burner rig oxidation resistance at 1700F for MA 754 and four other superalloys (Ref. 6)

Alloy	Weight Change (mg/cm²)		Metal Loss (mil) (b)	Maximum Attack (mil) (c)
	Undescaled	Descaled		
Inconel MA 754	-0.1	-7.4	0.79	3.11
IN 738	+1.4	-6.1	1.06	5.83
Mar-M 509	+0.9	-12.4	1.10	5.98
X40	-0.8	-9.6	1.18	5.71
Inconel 713C (a)	-386.0	-431.0	130	130

Note: Alloys tested for 168 hours in JP-5 fuel with 0.3 percent sulfur and 5 ppm sea water, air-to-fuel ratio 30 to 1, thermal cycled by rapid cool to room temperature every 60 minutes.
(a) Completely destroyed.
(b) Metal loss is loss of thickness due to oxide and sulfide scale formation.
(c) Maximum attack is metal loss plus additional loss in thickness due to internal oxidation and sulfidation.

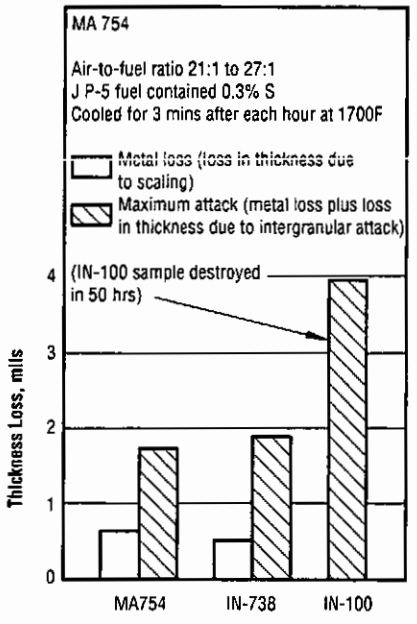

Fig. 2.3.4.9 Depth of metal loss and maximum attack after burner rig testing for 500 hours at 1700F for MA 754 and two other superalloys (Refs. 9, 22)

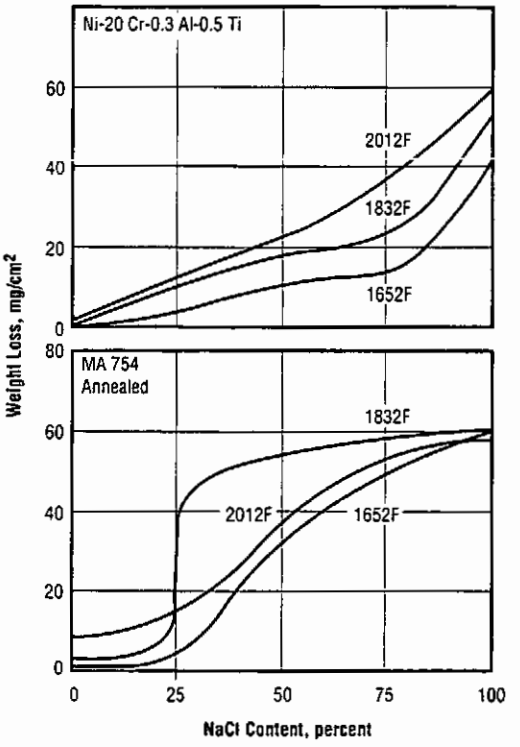

Fig. 2.3.4.10 Effects of salt composition and temperature on the corrosion weight loss of Ni-20Cr-0.3Al-0.5Ti and MA 754 alloys exposed for 16 hours in Na_2SO_4-NaCl mixtures (Ref. 23)

Table 3.2.3.1 Effects of orientation on impact energy at room temperature (Ref. 6)

Alloy: MA 754 (a)	
Specimen Orientation (b)	**Charpy-V Impact Energy (ft-lb)**
L-S	51.0
L-T	38.5
T-S	23.0
T-L	28.0

(a) Thermo-mechanically processed bar, annealed 1 hour at 2400F and air cooled.
(b) Notations according to ASTM E 399-74.

Table 3.2.7.1.1 Effects of notches on room temperature tensile properties in helium and in hydrogen (Ref. 6)

Alloy: MA 754 (a)							
Specimen Surface	**Atmosphere (b)**	**Orientation**	**F_{ty} (ksi)**	**F_{tu} (ksi)**	**e (percent)**	**RA (percent)**	**H_2/He Strength Ratio**
Smooth	He	L	90.4	145.2	23.0	47.0	-
		T	82.8	125.5	28.0	35.8	-
	H_2	L	72.3	124.4	12.8	8.7	0.86
		T	62.0	101.6	18.2	9.6	0.81
Notched (c)	He	L	-	170.5	-	5.0	-
		T	-	167.5	-	5.7	-
	H_2	L	-	163.5	-	4.9	0.96
		T	-	157.5	-	4.5	0.94

(a) Thermo-mechanically processed bar, annealed 1 hour at 2400F and air cooled.
(b) Gas pressure 5000 psi. Properties in helium are identical to those in air at atmospheric pressure.
(c) Notch dimensions not reported.

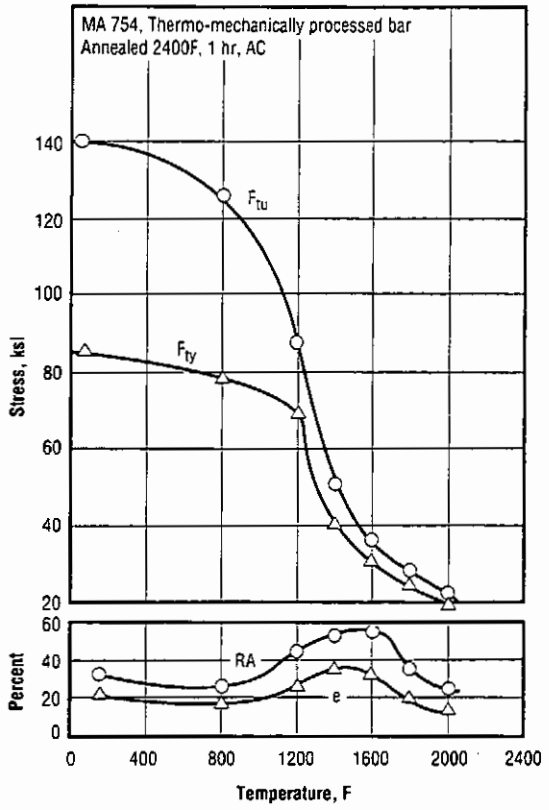

Fig. 3.3.1.1 Longitudinal tensile properties of thermo-mechanically processed bar (Ref. 6)

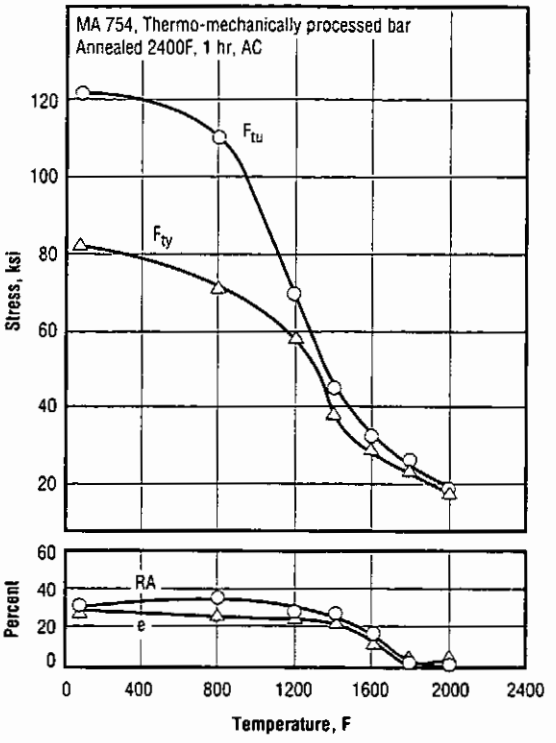

Fig. 3.3.1.2 Long transverse tensile properties of thermo-mechanically processed bar (Ref. 6)

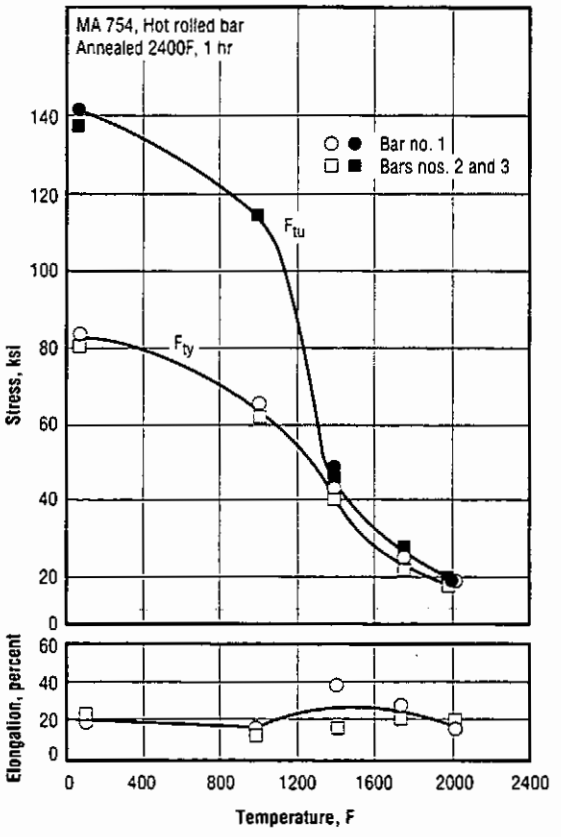

Fig. 3.3.1.3 Longitudinal tensile properties of hot rolled and annealed bar (Ref. 14)

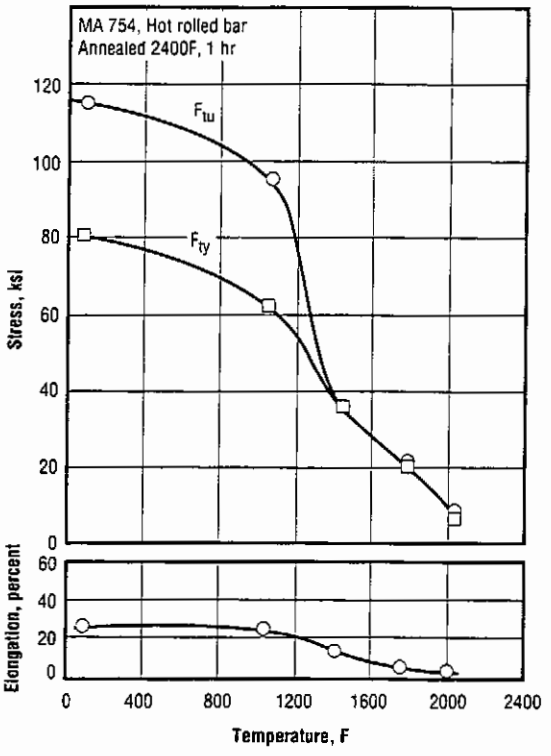

Fig. 3.3.1.4 Transverse tensile properties of hot rolled and annealed bar (Ref. 14)

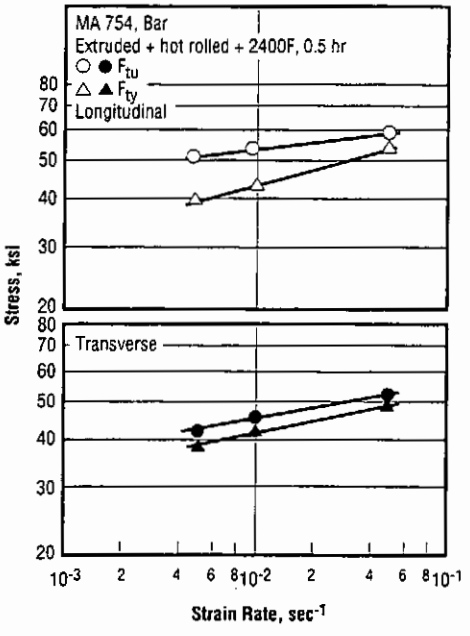

Fig. 3.3.1.6 Effects of strain rate and orientation on tensile strength at 1400F (Ref. 50)

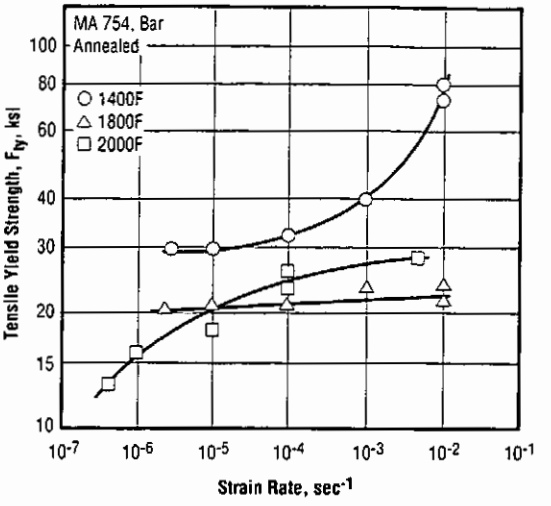

Fig. 3.3.1.5 Effects of strain rate and temperature on yield strength (Ref. 49)

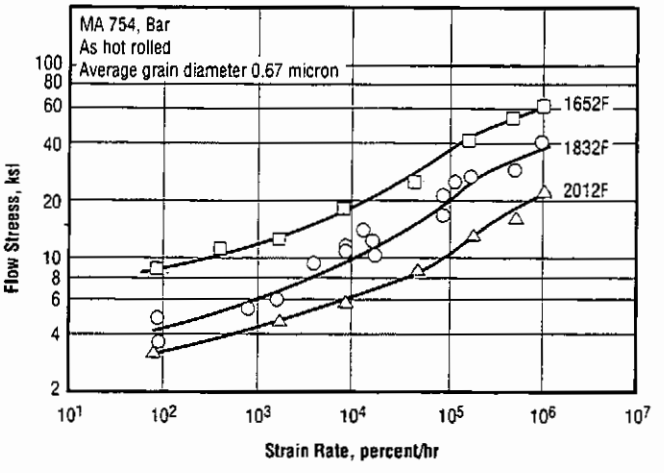

Fig. 3.3.1.7 Effects of strain rate and temperature on flow stress of fine-grained MA 754 (Ref. 25)

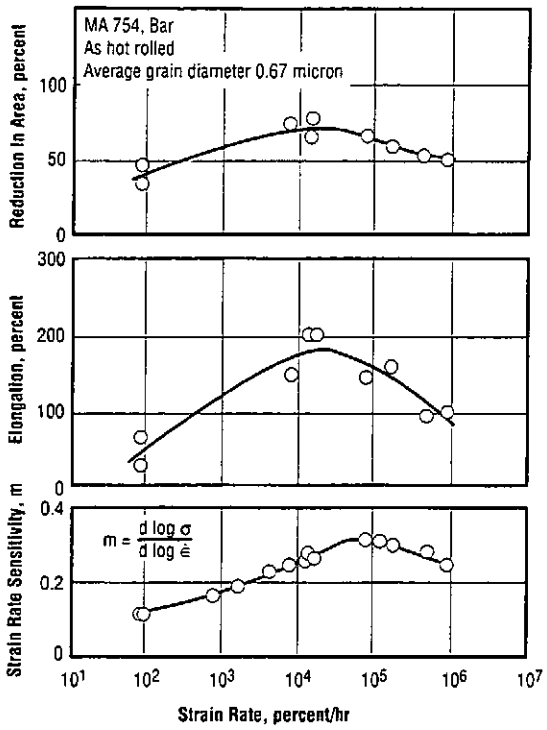

Fig. 3.3.1.8 Effects of strain rate on strain rate sensitivity and ductility for fine-grained MA 754 at 1832F (Ref. 25)

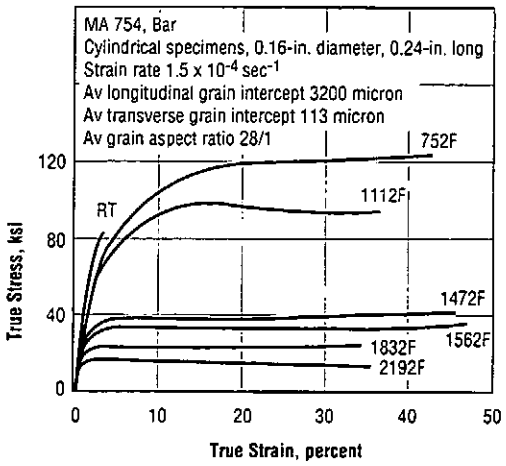

Fig. 3.3.2.1 Compression stress-strain curves at room and elevated temperatures (Ref. 26)

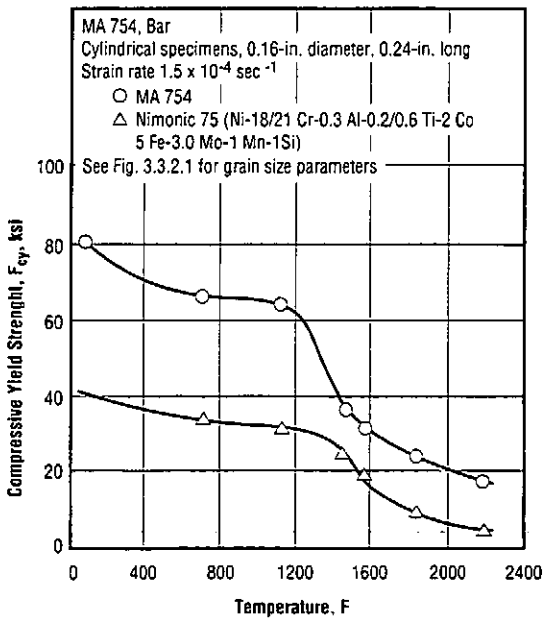

Fig. 3.3.2.3 Effects of temperature on compressive 0.2-percent yield strengths of MA 754 and of non-ODS alloy Nimonic 75 (Ref. 26)

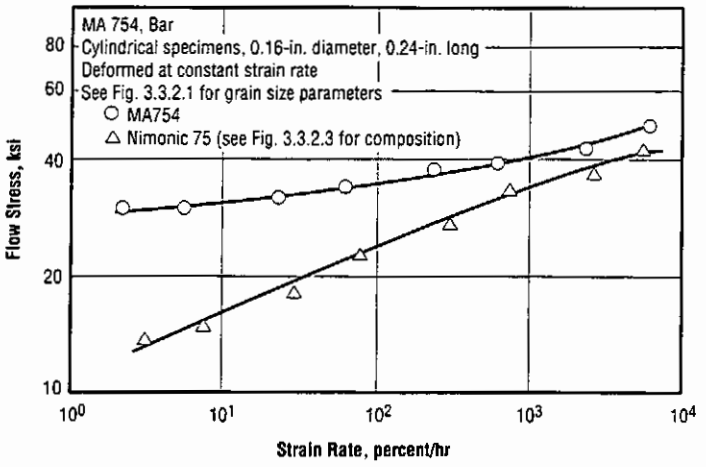

Fig. 3.3.2.4 Effects of strain rate on steady-state flow stress in compression at 1562F for MA 754 and non-ODS alloy Nimonic 75 (Ref. 26)

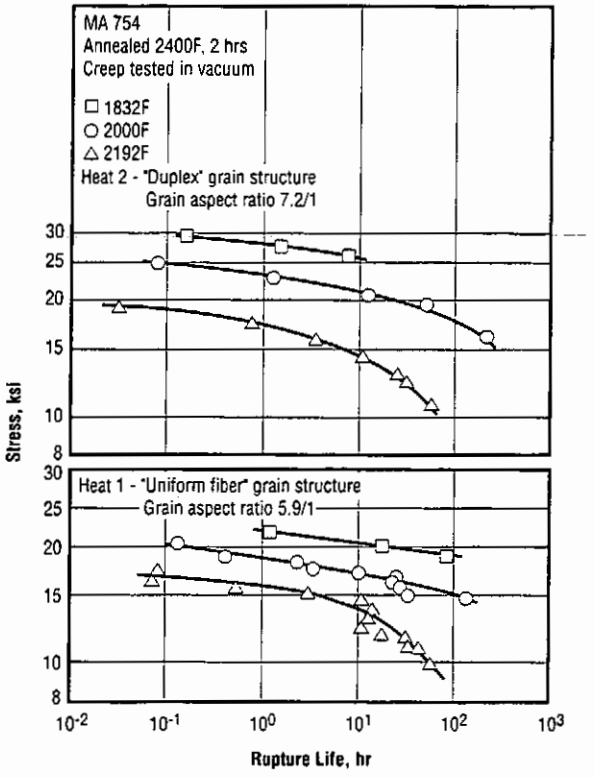

Fig. 3.4.1 Effects of temperature and grain structure on stress-rupture behavior of two heats of MA 754 (Ref. 31)

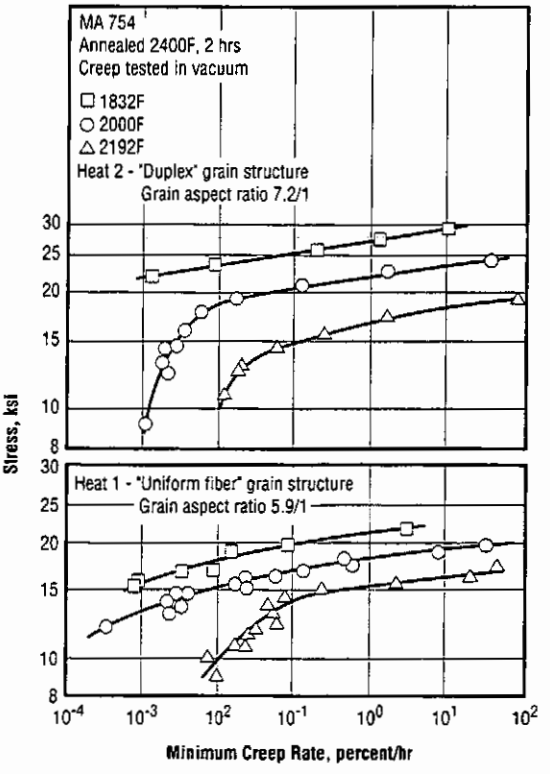

Fig. 3.4.2 Effects of temperature and grain structure on creep behavior of two heats of MA 754 (Ref. 31)

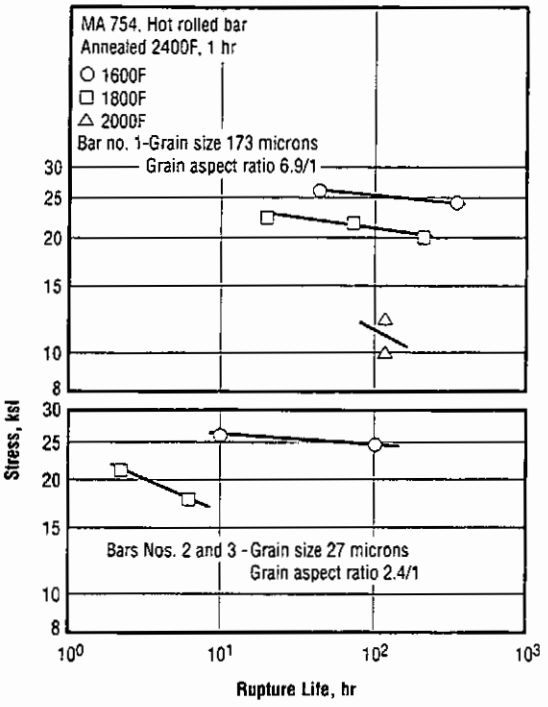

Fig. 3.4.3 Effects of temperature and grain structure on stress-rupture behavior of two bars of MA 754 (Ref. 14)

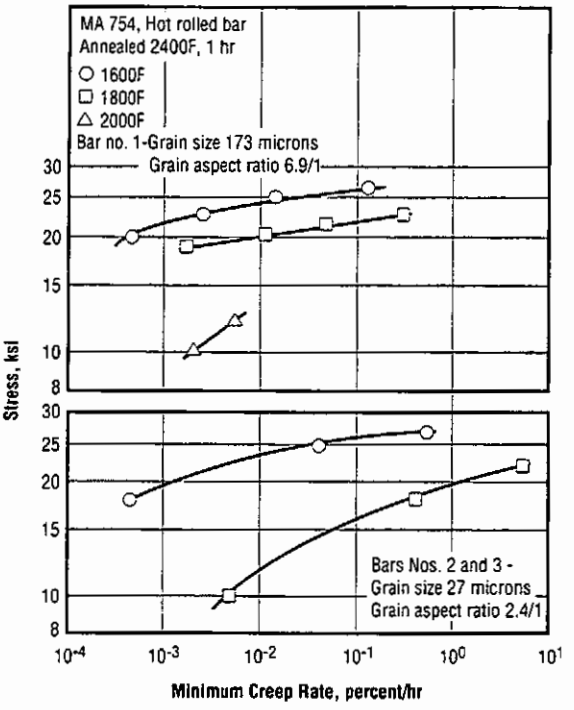

Fig. 3.4.4 Effects of temperature and grain structures on creep behavior of two bars of MA 754 (Ref. 14)

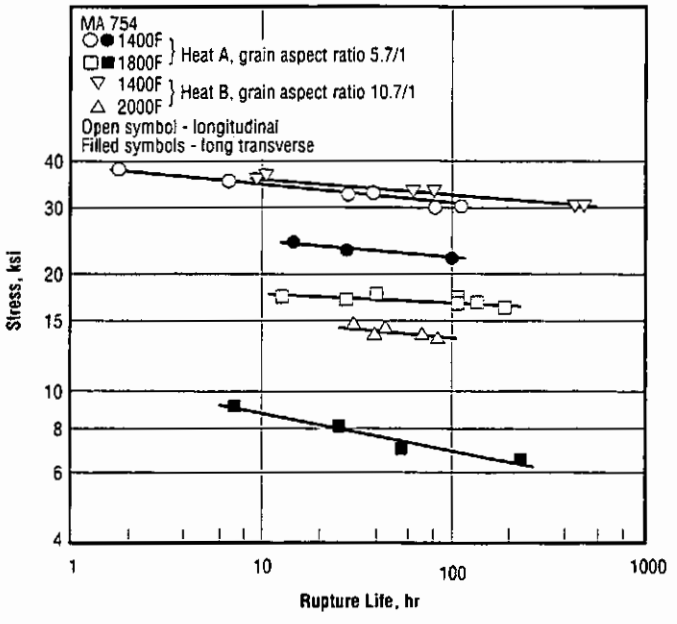

Fig. 3.4.5 Effects of temperature and orientation on stress-rupture behavior of two heats of MA 754 (Ref. 32)

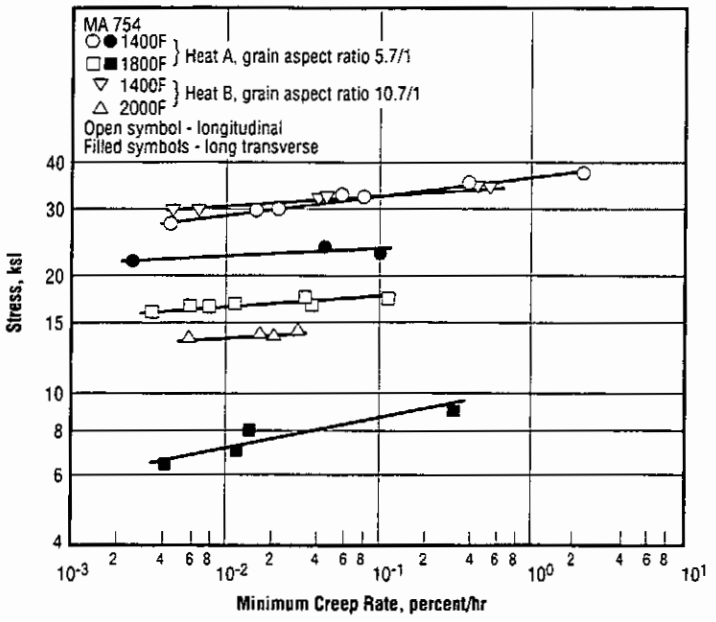

Fig. 3.4.6 Effects of temperature and orientation on creep behavior of two heats of MA 754 (Ref. 32)

Table 3.4.7 Longitudinal and long transverse stress-rupture properties (Ref. 6)

Alloy: MA 754 (a)						
Temperature (F)	Stress (ksi) to Produce Rupture in					
	100 Hours		1000 Hours		10,000 Hours (c)	
	L (b)	LT	L	LT	L	LT
1200	41.2	35.0	37.2	30.2	33.6	26.1
1400	31.1	25.0	28.8	21.6	26.6	18.6
1600	24.7	15.6	22.9	13.2	21.3	11.2
1800	19.7	9.1	18.7	6.6	17.8	4.8
2000	14.8	5.5	13.6	3.5	12.4	2.3
2100	13.1	3.4	11.3	2.4	9.7	1.6

(a) Thermo-mechanically processed bar, annealed 1 hour at 2400F and air cooled.
(b) "L" denotes longitudinal orientation, "LT" denotes long transverse orientation.
(c) Extrapolated.

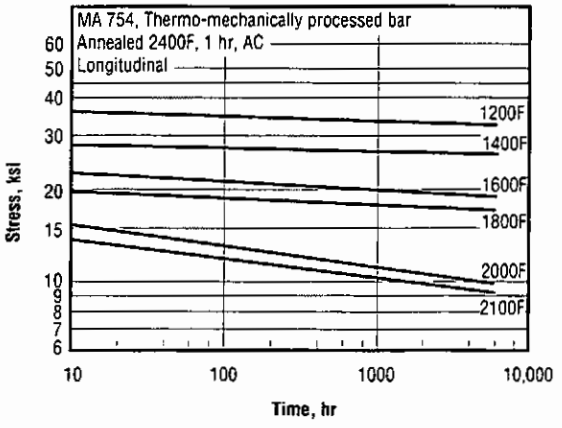

Fig. 3.4.8 Time to 0.5 percent creep strain (Ref. 6)

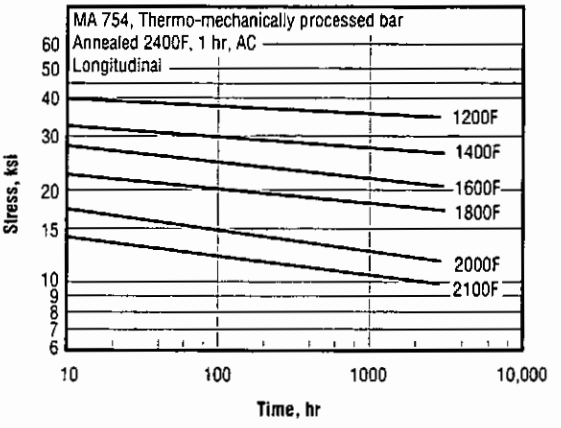

Fig. 3.4.9 Time to 1.0 percent creep strain (Ref. 6)

Table 3.4.10 Elevated temperature stress-rupture strength of MA 754 and other superalloys (Ref. 8)

Alloy	Stress (ksi) to Produce Rupture in 1000 Hours at Indicated Temperature			
	1600F	1800F	2000F	2200F
Nimonic 75	1.0	0.5	0.3	-
Inconel MA 754	22.9	18.7	13.6	9.0
Incoloy MA 956	12.0	9.7	7.4	4.5
Inconel 617	9.2	3.8	1.5	-

(Heat treatments not specified)

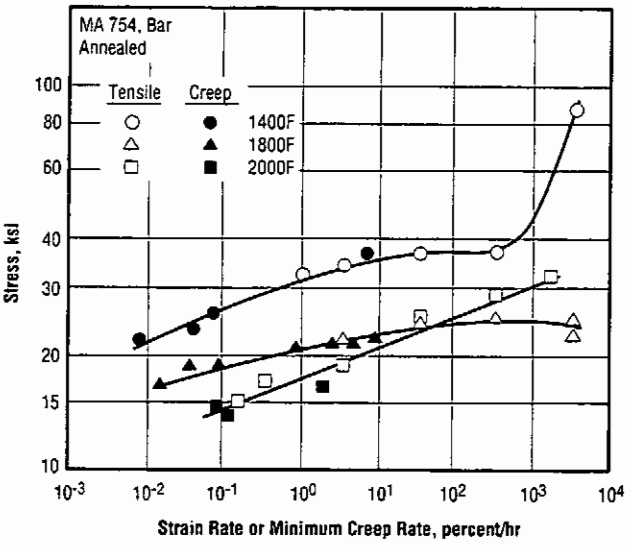

Fig. 3.4.11 Similarity of creep and tensile flow behavior at elevated temperatures (Ref. 49)

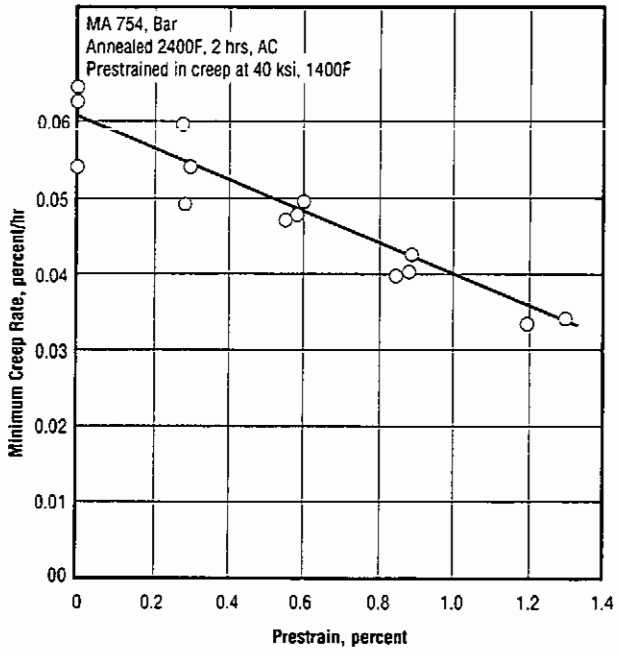

Fig. 3.4.12 Effects of prestraining on minimum creep rate at 32.5 ksi and 1400F (Ref. 34)

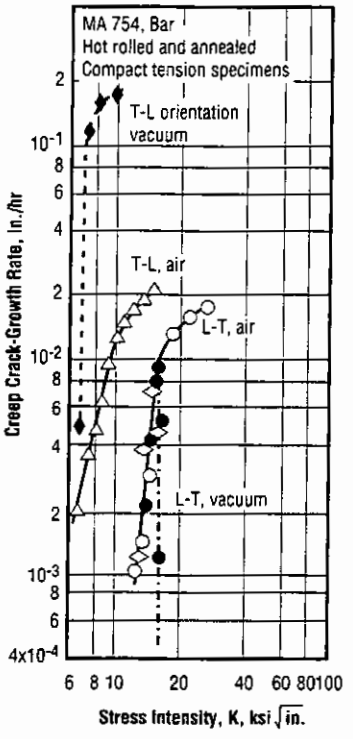

Fig. 3.4.13 Effects of orientation and environment on creep crack-growth rate at 1832F (Ref. 35)

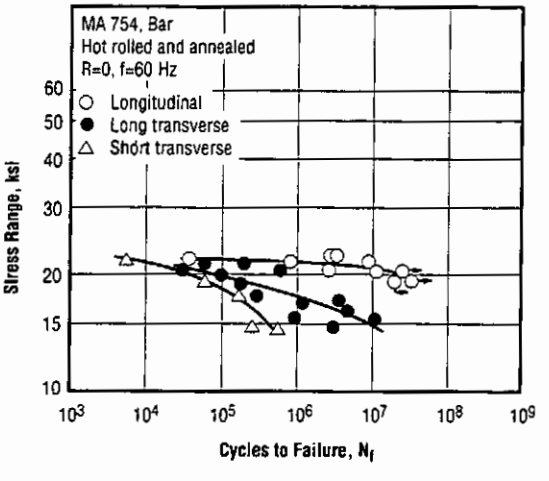

Fig. 3.5.1.1 Effects of specimen orientation on high-cycle fatigue behavior at 1562F (Ref. 36)

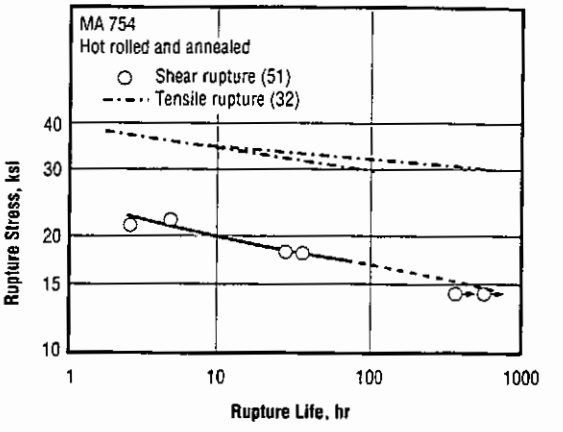

Fig. 3.4.14 Shear and tensile rupture strengths at 1400F (Refs. 32, 51)

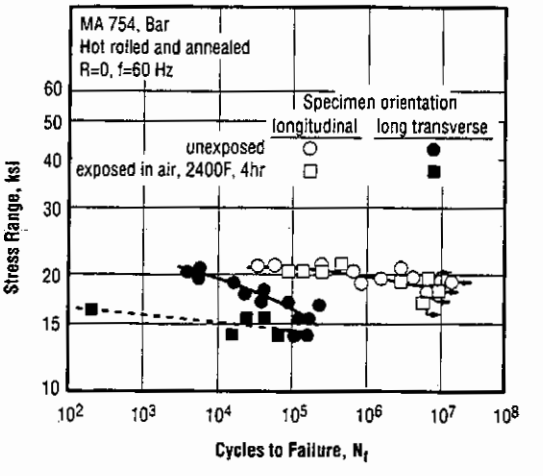

Fig. 3.5.1.2 Effects of high temperature air exposure on high-cycle fatigue behavior at 1562F for two specimen orientations (Ref. 36)

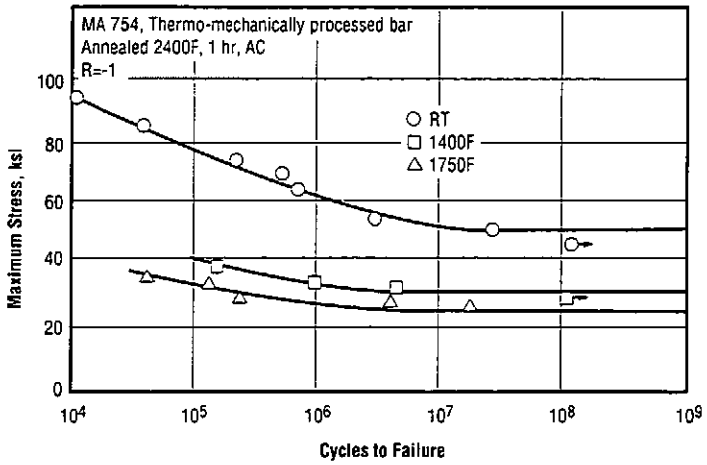

Fig. 3.5.1.3 Longitudinal rotating-beam fatigue strength (Ref. 6)

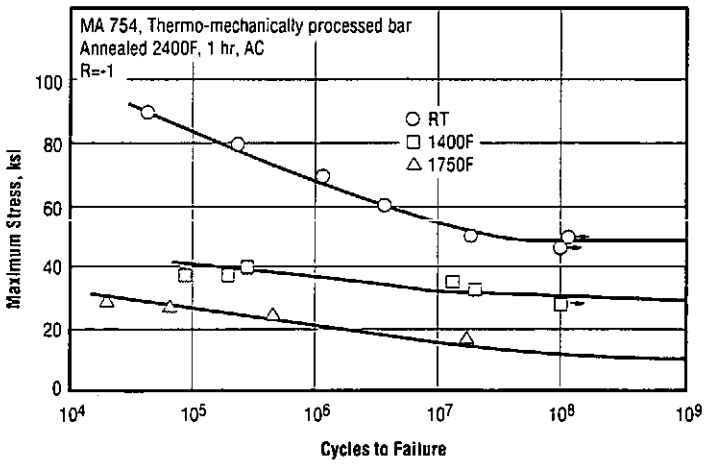

Fig. 3.5.1.4 Long transverse rotating-beam fatigue strength (Ref. 6)

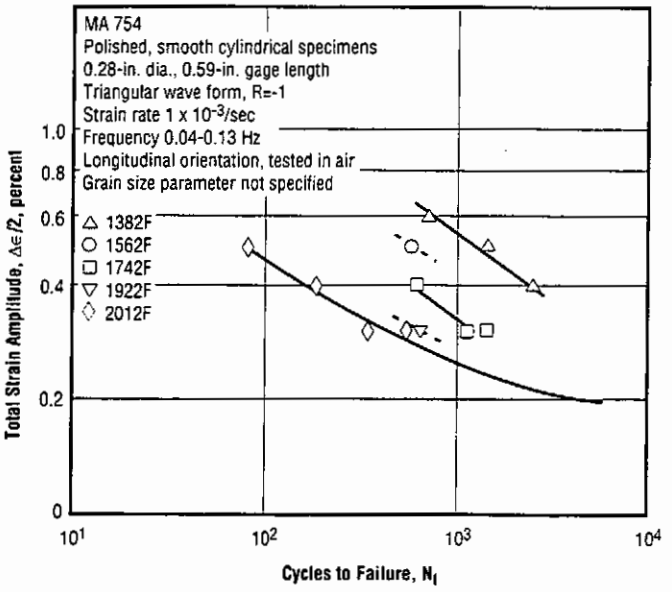

Fig. 3.5.2.1 Effect of temperature on low-cycle fatigue behavior (Ref. 38)

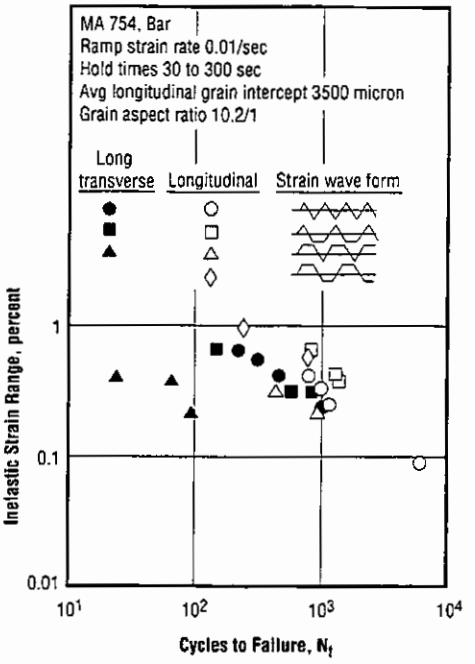

Fig. 3.5.2.2 Effects of specimen orientation and strain wave form on low-cycle fatigue behavior at 1562F (Ref. 39)

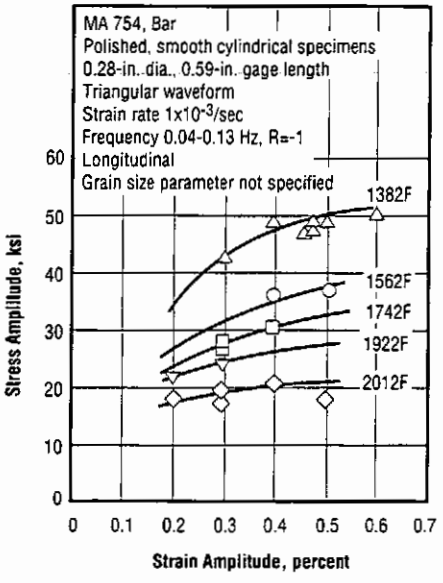

Fig. 3.5.2.3 Cyclic stress-strain curves (Ref. 38)

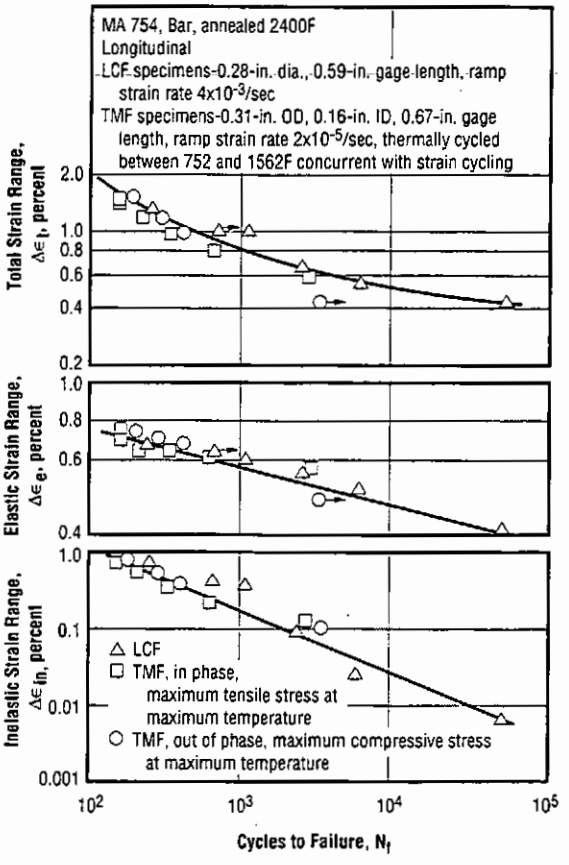

Fig. 3.5.2.4 Low-cycle fatigue behavior at 1562F and thermal-mechanical fatigue behavior at 752 to 1562F (Ref. 40)

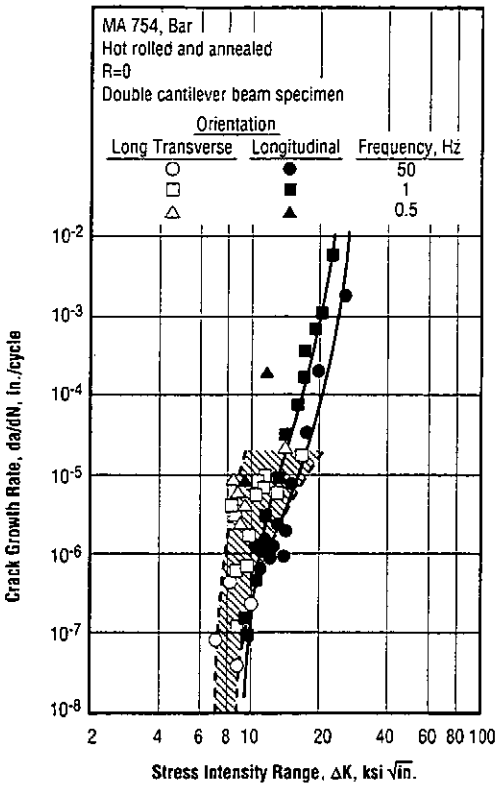

Fig. 3.5.3.1 Effects of cycle frequency and specimen orientation on fatigue crack-growth rates at 1562F (Ref. 37)

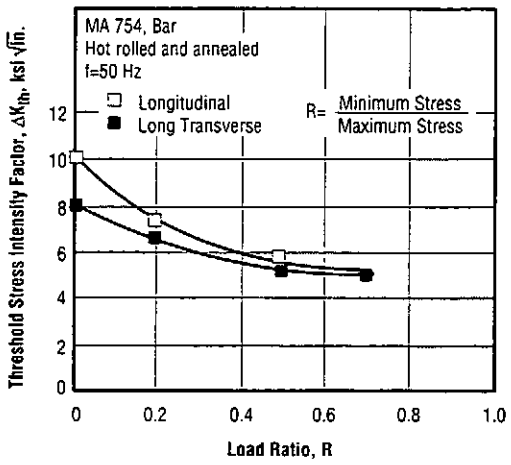

Fig. 3.5.3.2 Effects of load ratio and specimen orientation on threshold stress intensity factor for fatigue crack propagation at 1652F (Ref. 36)

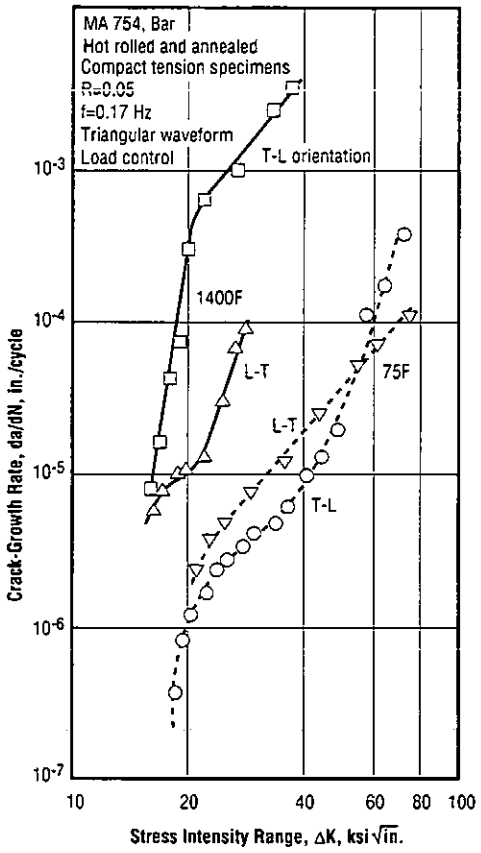

Fig. 3.5.3.3 Effects of temperature and specimen orientation on fatigue crack-growth rates in air (Ref. 35)

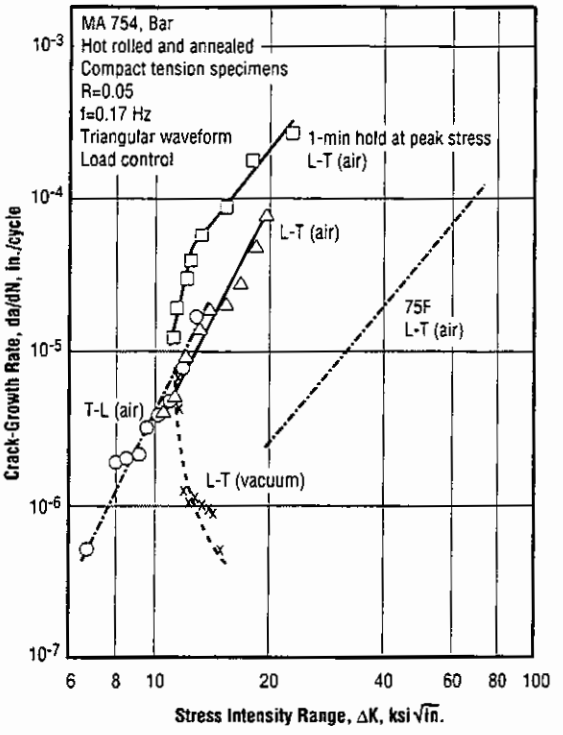

Fig. 3.5.3.4 Effects of hold time, environment, and orientation on fatigue crack-growth rates at 1832F (Ref. 35)

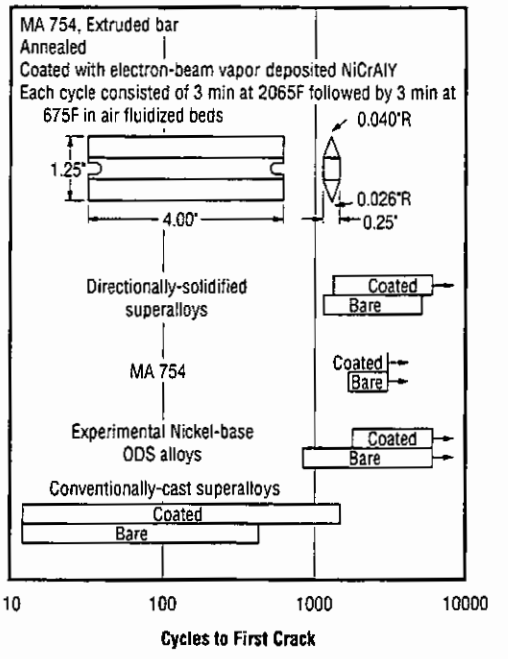

Fig. 3.5.4.1 Thermal fatigue behavior at 2065F for MA 754 compared with all other types of superalloys (Ref. 41)

Table 3.5.4.2 Thermal fatigue behavior at 1787 and 1967F for MA 754 compared to two other superalloys (Ref. 43)

Alloy (a)	Cycles to 0.04-in. Crack Length		Final Crack Length (in.)		
	Trans.	Long.	Longest Trans.	Longest Long.	Notch Crack
	2000 Cycles (b) RT to 1787F				
MA 754	500	40	.198	.255	.153
DS X-40	480	550	.250	.220	.220
DS René 150	>2000	1300	0	.080	.060
	600 Cycles (b) RT to 1967F				
MA 754	150	25	.159	.300	.155
DS X-40	150	80	.216	.204	.228
DS René 150	400	330	.047	.095	.095

(a) DS denotes directionally solidified. René 150 composition: Ni-10Co-5Cr-1Mo-6Ta-2.2V-3Re-1.5Hf-5.5Al-0.2Zr-0.06C-0.02B (pct).
(b) Each cycle consisted of 4 min. at 1787 or 1967F followed by 2 min. at RT in fluidized beds.

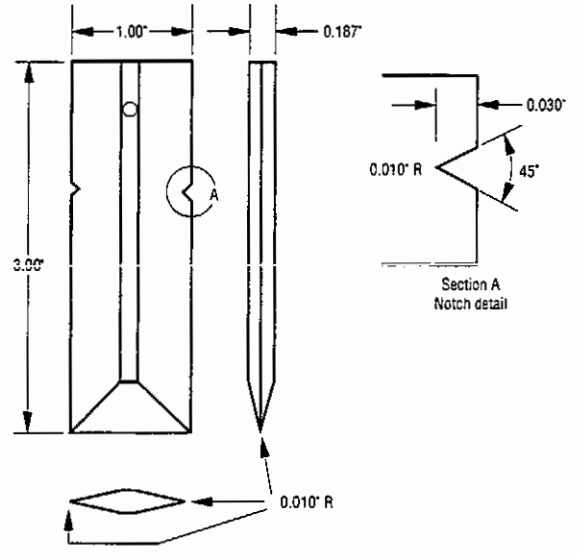

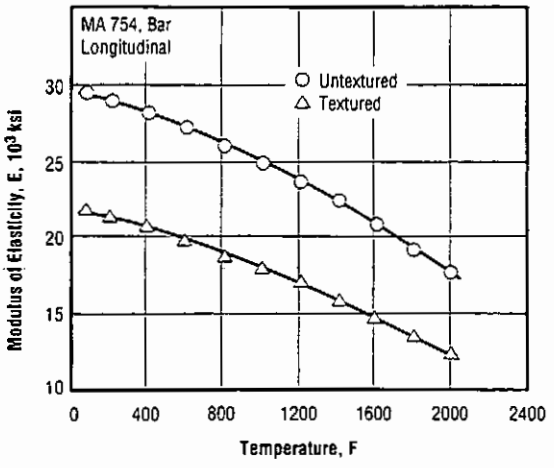

Fig. 3.6.2.1 Modulus of elasticity as a function of temperature (Ref. 6)

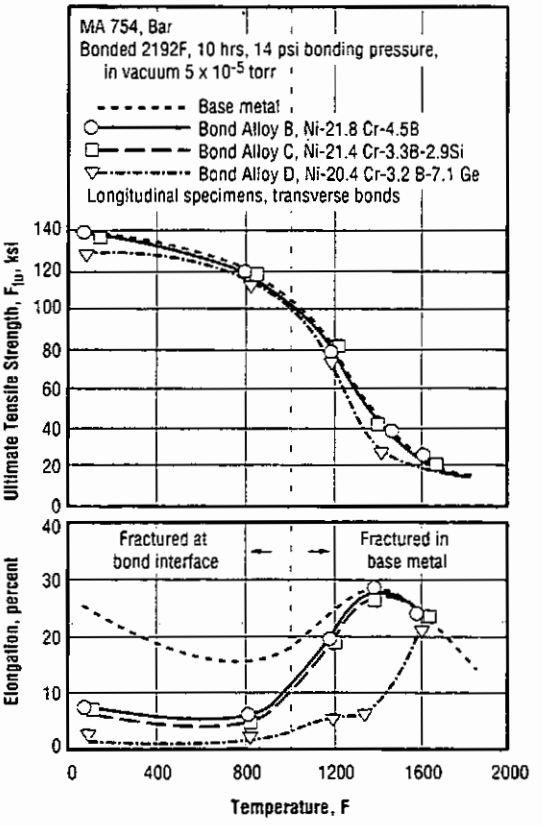

Fig. 4.3.1 Effects of temperature on tensile strength and elongation of liquid phase diffusion bonded alloy (Refs. 45, 46)

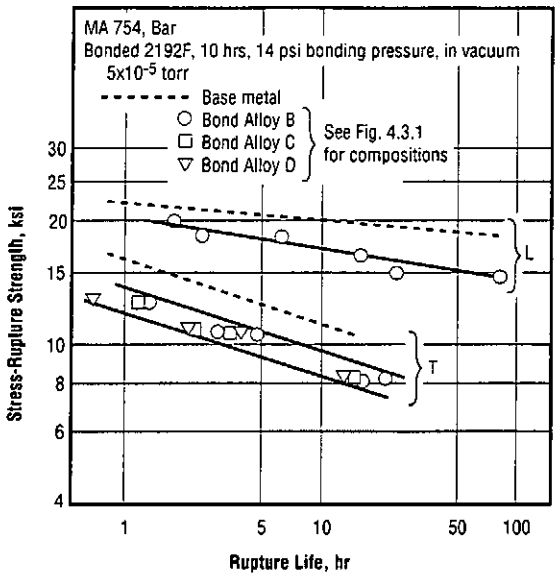

Fig. 4.3.2 Stress-rupture strength of liquid phase diffusion bonded alloy at 1800F (Ref. 45)

Table 4.3.3 Stress-rupture properties of brazed joints (Ref. 47)

Alloy: MA 754					
Brazing		**Stress Rupture**			
Alloy (a)	**Temperture (F) (b)**	**Temperature (F)**	**Stress (ksi)**	**Time (hr)**	**Fracture Location**
AM788	2300	1800	14	1000	(No fracture)
			16	168.4	Braze and base alloy
		2000	5	1000	(No fracture)
			6	178.2	Braze
			4/6/8	24/24/21	Braze
B93	2300	1800	2/4/6/8/10	24/24/24/24/1051	(No fracture)
			12	1000	(No fracture)
			14	1000	(No fracture)
			16	392	Braze
TD6	2400	2000	8	105.5	Braze
			4/6/8/10	24/24/24/6.4	Braze

(a) Compositions of braze alloys, wt. pct.:
AM788: Co-21Ni-22Cr-14W-2Si-2B-0.03La
B93: Ni-14Cr-9.5Co-4Mo-4W-4.5Si-0.7B-3Al
TD6: Ni-16Cr-5Fe-17Mo-5W-4Si-1Al

(b) Brazed for 0.5 hr at temperature in 10^{-6} torr vacuum.

(c) "Tuning fork" stress rupture specimen

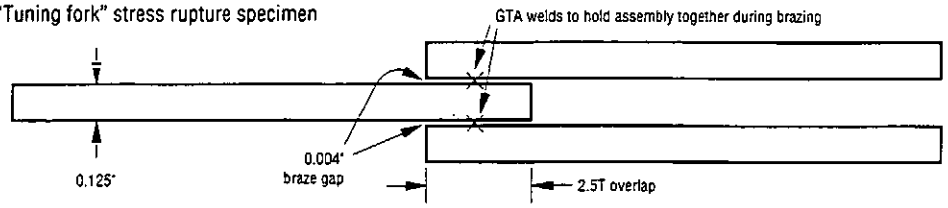

References

1. Hack, G. A. J., "Superalloys for the '80s," *Metallurgia*, Vol. 49, No. 6, pp. 256-257 (June 1982).
2. Fleetwood, M. J., "Mechanical Alloying - The Development of Strong Alloys," *Materials Science and Technology*, Vol. 2, No. 12, pp. 1176-1182 (December 1986).
3. Sundaresan, R., and Froes, F. H., "Mechanical Alloying," *Journal of Metals*, Vol. 39, No. 8, pp. 22-27 (August 1987).
4. Fischer, J. J., and Haeberle, R. M., "Commercial Status of Mechanically Alloyed Materials," presented at MPIF/APMI Conference on Modern Developments in Powder Metallurgy, Orlando, FL, Vol. 21, pp. 461-477 (June 5-10, 1988).
5. Grundy, E., "Structure and Properties of Forged ODS Nickel-Base Alloys," presented at Metal Powder Report International Conference on PM Aerospace Materials - 87, Lucerne, Switzerland, pp. 12.1-12.10 (November 2-4, 1987).
6. "Inconel Alloy MA 754," Trade Literature, INCO Alloys International, Huntington, WV 25720, 13 pp. (1992).
7. Hotzler, R. K., and Glasgow, T. K., "Recrystallization Characteristics of Oxide-Dispersion-Strengthened Nickel-Base Alloys," *Proceedings* of the Fourth International Symposium on Superalloys, Champion, PA, pp. 455-464 (September 21-25, 1980).
8. Fischer, J. J.; deBarbadillo, J. J.; and Shaw, M. J., "MA Alloys for Industrial Applications," *Proceedings*, ASM International Conference on Structural Applications of Mechanical Alloying, eds. F. H. Froes and J. J. deBarbadillo, pp. 79-87 (1990).
9. deBarbadillo, J. J., and Fischer, J. J., "Dispersion-Strengthened Nickel-Base and Iron-Base Alloys," *ASM Metals Handbook*, Tenth Edition, Vol. 2, pp. 943-949 (1990).
10. Wilson, R. K., and Perry, F. L., "Superior High Temperature Capabilities of MA Superalloys Developed by Thermomechanical and Heat Treatment Processes," *Industrial Heating*, Vol. 51, No. 5, pp. 27-30 (May 1984).
11. "Inconel Alloy MA 754," *Alloy Digest*, Filing Code NI-244 (March 1990).
12. Raghavan, M.; Klein, C.; and Petrovic-Luton, R., "Analytical Microscopic Investigation of Commercial Oxide-Dispersion-Strengthened Alloys," presented at 39th Annual Meeting, Electron Microscopy Society of American, Atlanta, GA, pp. 142-143 (August 10-14, 1981).
13. Stephens, J. J., and Spooner, S., "Determination of Dispersoid Size Distribution in Inconel MA 754 by Small-Angle X-Ray Scattering," *Acta Metallurgica*, Vol. 34, No. 2, pp. 303-312 (February 1986).
14. Ebert, L. J.; Telich, M. L.; Holly, M.; and Roopchand, B., "Cold-Working and Annealing Effects on the Creep and Rupture Resistance of the Oxide-Dispersion-Strengthened Alloy MA 754," TR-12896, US Army Tank - Automotive Command (November 1983).
15. Nickel, H., and Quadakkers, W. J., "Growth Mechanisms and Protective Properties of Chromia and Alumina Scales on Oxide-Dispersion-Strengthened Alloys," presented at ASM Conference on Heat-Resistant Materials, Fontana, WI, pp. 87-94 (September 23-26, 1991).
16. Quadakkers, W. J.; Speier, W.; Holzbrecher, H.; and Nickel, H., "SIMS Investigations of the Transport Phenomena in Chromia and Alumina Scales on ODS Alloys," presented at Conference on Microscopy of Oxidation, Cambridge, UK, pp. 149-160 (March 26-28, 1990).
17. Yurek, G. J.; Przybyiski, K.; and Garratt-Reed, A. J. "Segregation of Y to Grain Boundaries in Cr_2O_3 and NiO Scales Formed on an ODS Alloy," *Journal of the Electrochemical Society*, Vol. 134, No. 10, pp. 2643-2644 (October 1987).
18. Quadakkers, W., J.; Holzbrecher, H.; Briefs, K. G.; and Beske, H., "Differences in Growth Mechanisms of Oxide Scales Formed on ODS and Conventional Wrought Alloys," *Oxidation of Metals*, Vol. 32, No. 1/2, pp. 67-88 (August 1989).
19. Rosenstein, A. H.; Tien, J. K.; and Nix, W. D., "Void Formation in Inconel MA 754 by High Temperature Oxidation," *Metallurgical Transactions*, Vol. 16A, No. 8, pp. 1437-1444 (August 1985).
20. Lowell, C. E., and Barrett, C. A., "The Oxidation and Corrosion of ODS Alloys," NASA TM-102555 (June 1990).
21. Ramanarayanan, T. A.; Ayer, R.; Petrovic-Luton, R.; and Leta, D. P., "The Influence of Yttrium on Oxide Scale Growth and Adherence," *Oxidation of Metals*, Vol. 29, No. 5-6, pp. 445-472 (June 1988).
22. Smith, G. D., and Fischer, J. J., "High Temperature Corrosion Resistance of Mechanically Alloyed Products in Gas Turbine Environments," presented at the Gas Turbine and Aerospace Congress and Exposition, Brussels, Belgium (June 11-14, 1990).
23. Nishi, Y.; Shinata, Y.; and Araki, Y., "Hot Corrosion of Mechanical Alloy MA 754 Induced by Na_2SO_4-NaCl Mixtures," *Journal of the Iron and Steel Institute of Japan*, Vol. 69, No. 9, pp. 1198-1205 (July 1983).
24. Gregory, J. K., "Superplastic Deformation in Oxide Dispersion Strengthened Nickel-Base Superalloys," Dissertation, Stanford University, UMI Dissertation Information Service (1983).
25. Gregory, J. K.; Gibeling, J. C.; and Nix, W. D., "High Temperature Deformation of Ultra-Fine-Grained Oxide-Dispersion-Strengthened Alloys," *Metallurgical Transactions*, Vol. 16A, No. 5, pp. 777-787 (May 1985).

26. Reppich, B.; Listl, W.; and Meyer, T., "Particle-Strengthening Mechanisms in ODS Superalloys," presented at Conference on High Temperature Alloys for Gas Turbines and Other Applications 1986 - Part 2, Liege, Belgium, pp. 1023-1035 (October 6-9, 1986).

27. Stephens, J. J., Jr., "Creep and Fracture of a Yttria Dispersed Nickel-Chromium Alloy," Dissertation, Stanford University, UMI Dissertation Information Service (1985).

28. Stephens, J. J., and Nix, W. D., "Creep and Fracture of Inconel MA 754 at Elevated Temperatures," *Proceedings* of the 5th International Symposium on Superalloys, Superalloys 1984, Seven Springs Mountain Resort, Champion, PA, pp. 327-334 (October 7-11, 1984).

29. Stephens, J. J., and Nix, W. D., "The Effect of Grain Morphology on Longitudinal Creep Properties on Inconel MA 754 at Elevated Temperatures," *Metallurgical Transactions*, Vol. 16A, No. 7, pp. 1307-1324 (July 1985).

30. Herrick, R. S.; Weertman, J. R.; Petrovic-Luton, R.; and Luton, M. J., "Dislocation/Particle Interactions in an Oxide-Dispersion-Strengthened Alloy," *Scripta Metallurgica*, Vol. 22, No. 12, pp. 1879-1884 (December 1988).

31. Stephens, J. J., and Nix, W. D., "Constrained Cavity Growth Models of Longitudinal Creep Deformation of Oxide-Dispersion-Strengthened Alloys," *Metallurgical Transactions*, Vol. 17A, No. 2, pp. 281-293 (February 1986).

32. Howson, T. E.; Stulga, J. E.; and Tien, J. K., "Creep and Stress Rupture of Oxide-Dispersion-Strengthened Mechanically Alloyed Inconel Alloy MA 754," *Metallurgical Transactions*, Vol. 11A, No. 9, pp. 1599-1607 (September 1980).

33. Woodford, D. A., and Bricknell, R. H., "The Effect of High Temperature Air Exposure on the Stress Rupture Life of Nickel- and Cobalt-Base Superalloys," *Proceedings* of the Fourth International Symposium on Superalloys, Superalloys 1980, Champion, PA, pp. 633-641 (September 21-25, 1980).

34. Marlin, R. T.; Cosandey, F.; and Tien, J. K., "The Effect of Predeformation on the Creep and Stress Rupture of an Oxide-Dispersion-Strengthened Mechanical Alloy," *Metallurgical Transactions*, Vol. 11A, No. 11, pp. 1771-1775 (November 1980).

35. Shahinian, P., and Sadananda, K., "Fatigue and Creep Crack Growth in Oxide-Dispersion-Strengthened MA 754," *Metallurgical Transactions*, Vol. 21A, No. 1, pp. 177-187 (January 1990).

36. Nazmy, M. Y., and Singer, R. F., "High Cycle Fatigue and Fatigue Crack Growth of the Oxide-Dispersion-Strengthened Alloy MA 754," *Metallurgical Transactions*, Vol. 16A, No. 8, pp. 1437-1444 (August 1985).

37. Nazmy, M. Y.; Singer, R. F.; and Wuthrich, C., "Fatigue Crack Propagation in MA 754 Oxide-Dispersion-Strengthened Alloy," *Proceedings* of the 2nd International Conference on Fatigue and Fatigue Thresholds, Fatigue 84 - Volume 1, University of Birmingham, UK, pp. 381-389 (September 3-7, 1984).

38. Elzey, D. M., and Arzt, E., "Crack Initiation and Propagation During High-Temperature Fatigue of Oxide-Dispersion-Strengthened Superalloys," *Metallurgical Transactions A*, Vol. 22A, No. 4, pp. 837-851 (April 1991).

39. Nazmy, M. Y., "High-Temperature Low Cycle Fatigue Behavior and Lifetime Prediction of a Nickel-Base ODS Alloy," *Proceedings* of Symposium on Low Cycle Fatigue, Bolton Landing, NY, ASTM-STP-942, pp. 385-398 (September 30 - October 4, 1985).

40. Henderson, P.; Lindblom, J.; and Ivarsson, B., "Thermo-Mechanical and Low Cycle Fatigue Behavior of MA 754," presented at Conference on High Temperature Materials for Power Engineering 1990, II, Liege, Belgium, pp. 1151-1162 (September 24-27, 1990).

41. Whittenberger, J. D., and Bizon, P. T., "Comparative Thermal Fatigue Resistance of Several Oxide-Dispersion-Strengthened Alloys," *International Journal of Fatigue*, Vol. 3, No. 4, pp. 173-180 (October 1981).

42. Hofer, K. E.; Hill, V. L.; and Humphreys, V. E., "Thermal Fatigue and Oxidation Data of Oxide-Dispersion-Strengthened Alloys," NASA CR-159842 (March 1980).

43. Woodford, D. A., "Thermal Fatigue Testing of Gas Turbine Materials," *Proceedings* of Third International Conference on Mechanical Behavior of Materials, Cambridge, England, pp. 33-42 (August 20-24, 1979).

44. Grundy, E.; Precious, C. J.; and Pinder, D., "Hot Forming of Mechanically Alloyed Gas Turbine Components," *Metal Powder Reports*, Vol. 40, No. 10, pp. 565-569 (October 1985).

45. Hirane, T.; Morimoto, S.; and Funamoto, T., "Liquid Phase Diffusion Bonding of a Nickel-Base Oxide-Dispersion-Strengthened Alloy MA 754," *Journal of the Iron and Steel Institute of Japan*, Vol. 72, No. 10, pp. 1590-1597 (August 1986).

46. Hirane, T.; Morimoto, S.; Sasaki, T.; and Funamoto, T., "Properties of Liquid Phase Diffusion Bonded Oxide-Dispersion-Strengthened Nickel-Base Alloy at Elevated Temperature," *Transactions of the Iron and Steel Institute of Japan*, Vol. 24, No. 12, p. B-408 (December 1984).

47. Kelly, T. J., "Brazing of Inconel Alloy MA 754 for High Temperature Applications," *Welding Journal*, Vol. 6, No. 10, pp. 317-s-319-s (October 1982).

48. Elder, J. E.; Thamburaj, R.; and Patnaik, P. C., "Braze Repair of MA 754 Aero Gas Turbine Engine Nozzles," presented at 1989 ASME Conference on Turbo Expo - Land, Sea, and Air, Toronto, Ontario, Canada (June 5-8, 1989).

49. Jacobs, E. G., "Understanding the Stress-Resisting Creep and Hot Tensile Deformation on ODS Superalloys," Dissertation, Columbia University, UMI Dissertation Information Service (1990).

50. Anglin, A. E., Jr., "Transverse and Longitudinal Tensile Properties at 760C of Several Oxide-Dispersion-Strengthened Nickel-Base Alloys," NASA TM-79189 (1979).

51. Glasgow, T. K., "Creep Shear Behavior of the Oxide-Dispersion-Strengthened Superalloy MA 6000E," NASA TM-82704 (1981).